Atmos. Chem. Phys. Discuss., 11, 1971–2023, 2011
www.atmos-chem-phys-discuss.net/11/1971/2011/
doi:10.5194/acpd-11-1971-2011

Atmospheric Chemistry and Physics Discussions

Explicit cloud-top entrainment parameterization in the global climate model ECHAM5-HAM

C. Siegenthaler-Le Drian[1], **P. Spichtinger**[2], **and U. Lohmann**[1]

[1]Institute for Atmospheric and Climate Science, ETH Zurich, 8092 Zurich, Switzerland
[2]Institute for Atmospheric Physics, Johannes Gutenberg University Mainz, 55128 Mainz, Germany

Received: 1 December 2010 – Accepted: 7 January 2011 – Published: 20 January 2011

Correspondence to: C. Siegenthaler-Le Drian (colombe.ledrian@env.ethz.ch)

Published by Copernicus Publications on behalf of the European Geosciences Union.

Abstract

New developments in the turbulence parameterization in the general circulation model ECHAM5-HAM are presented. They consist mainly of an explicit entrainment closure at the top of stratocumulus-capped boundary layers and the addition of an explicit contribution of the radiative divergence in the buoyancy production term. The impact of the new implementations on a single column model study and on the global scale is presented here. The parameterization has a "smoothing" effect: the abnormally high values of turbulence kinetic energy are reduced, both in the single column and in the Californian stratocumulus region. A sensitivity study with prescribed droplet concentration shows a reduction in the sensitivity of liquid water path to increasing cloud aerosol optical depth. We also study the effect of the new implementation on a Pacific cross-section. The entrainment parameterization leads to an enhanced triggering of the convective activity.

1 Introduction

One aim of climate modeling is to project the future climate in a representative way, using different anthropogenic emissions scenarios. In this context, marine boundary layer clouds have proven to be a key issue. Indeed, experiments with doubling CO_2 emissions show quite different responses of low-level clouds between the different existing climate models (Bony and Dufresne, 2005; Stephens, 2005, etc.). Because stratocumuli have a strong impact on the radiative budget (Hartmann et al., 1992), the predicted climates strongly depend on their evolution.

Different field campaigns showed that stratocumuli experience a diurnal cycle even if the sea surface temperature remains more or less constant (FIRE – Hignett, 1991; Blaskovic et al., 1991, ASTEX – Ciesielski et al., 2001, EPIC – Bretherton et al., 2004). The cloud thickness and coverage show an early afternoon minimum and early morning maximum. This is important for stratocumulus feedbacks from a climate point of

ACPD
11, 1971–2023, 2011

view, as the clouds are then the thinnest and less reflective when the shortwave radiation is the strongest (Bretherton et al., 2004). During night, when the radiative cooling is not compensated by the shortwave heating, the temperature of the top of the cloud decreases, inducing strong mixing. The planetary boundary layer (PBL) is then well-mixed, gets colder and moister. During the same time, the increased longwave (LW) cooling induces more cloud-top entrainment. As the height of the PBL is the result of the competition between large-scale subsidence and cloud top entrainment, the PBL top rises and the cloud thickens. During daytime, the longwave radiative cooling efficiency to generate turbulence at the top of the cloud is reduced. The PBL tends to decouple, which means an inhibition of the transport of moisture and temperature across the PBL. The cloud-top entrainment is reduced and the cloud top lowers (Sandu, 2007). This description is a simplified picture, the interaction with precipitation complicates the story, as well as the large-scale dynamics. As an example, the cloud diurnal cycle during the EPIC and campaign was correlated with a subsidence diurnal cycle (Bretherton et al., 2004). A diurnal cycle in drizzle was also observed during both EPIC and DYCOMS-II campaigns, with substantial drizzle during the late night and early morning, and lower drizzle rates during daytime (Bretherton et al., 2004; van Zanten et al., 2005).

Aerosol-cloud interactions and the influence of anthropogenic aerosols on clouds and climate remain an area of active research. Twomey (1977) hypothesizes that, for the same liquid water content, an increased aerosol number would result in more but smaller droplets. Albrecht (1989) stated that these smaller droplets are less likely to grow to precipitation size drops. Thus, the lifetime and liquid water path (LWP) of the clouds is expected to increase in polluted cases. A suppression of precipitation can induce dynamic feedbacks affecting in turn the LWP, for example enhanced entrainment of warm dry air into the PBL at the cloud top. Indeed, recent nocturnal large eddy simulation (LES) studies show that entrainment at the cloud top of the marine boundary layer is very important in regulating the cloud liquid water content under polluted conditions (Ackermann et al., 2004; Stevens et al., 2005). In a theoretical study, Wood

ACPD
11, 1971–2023, 2011

(2007) concluded that on small time scales (lower than a few days) cloud thinning can occur when the number of droplets increases. More recently, Sandu et al. (2008) emphasized the reduction of the LWP in a polluted environment, due to the interaction between entrainment, solar radiation, drizzle evaporation and sensible heat flux; their simulations even suggest this response to be irrespective of the large-scale forcing. In the meantime, Hill et al. (2008) pointed out that ignoring the change in LWP due to the evaporation-entrainment feedback associated with increasing cloud condensation nuclei concentrations (CCN) can result in a significant overestimation of the aerosol indirect forcing.

The complex interactions affecting cloud lifetime and LWP are not captured in the various general circulation models (GCM). Quaas et al. (2009), in a climate model intercomparison, showed an overestimation of the positive correlation of LWP with aerosol optical depth (AOD) by a factor of two compared to MODIS satellite data for almost all participating models. As the authors suggest, the overestimation might be due to inappropriate autoconversion parameterizations, but the crude representation of planetary boundary layer (PBL) dynamics, particularly the inclusion of cloud-top entrainment may be another issue.

The direct effect of cloud-top entrainment is to deepen, dry and warm the PBL. In reaction to aerosol loading, it is thought that sedimentation of cloud drops will reduce cloud-top entrainment (or its efficiency) (Ackermann et al., 2004; Stevens et al., 2005; Bretherton et al., 2007). But the interactions within the PBL are quite complex. For example, an enhanced entrainment could also induce larger moisture fluxes, thus more water vapor entering the PBL, and maybe more clouds. Different surface fluxes will lead to a completely different evolution of the simulation (Sandu et al., 2009). Therefore it is important to model cloud-top entrainment accurately in order to simulate a realistic evolution of the marine PBL.

ECHAM5 uses an e-l turbulent scheme, with a prognostic turbulence kinetic energy (TKE) e and a diagnostic length scale l. As shown by Lenderink et al. (2000), e-l turbulent closure reproduces the main features of vertical mixing and entrainment in

ACPD
11, 1971–2023, 2011

stratocumulus-capped boundary layers in LES resolution well. Nevertheless, by studying the turbulent scheme of ECHAM4, they showed that its performance diminishes when the resolution decreases and the different fluxes and TKE are not represented satisfactorily in the L31 resolution (31 vertical levels). Moreover, the difficulty of resolving the buoyancy profile in a coarse grid can lead to substantial errors in the predicted TKE profile (Bretherton and Park, 2009). When ECHAM5 is coupled to the HAM aerosol scheme, the CPU time increases considerably so that it is run at a rather coarse horizontal and vertical resolution of T63L31. In order to overcome the deficiency of the *e*-*l* turbulent scheme with this resolution, we replace the TKE diffusion by an explicit entrainment closure at the top of marine stratocumulus-capped boundary layers. Some other GCMs are using a cloud-top entrainment parameterization inside their turbulent scheme (Lock, 1998; Köhler, 2005). Moreover, recently, Bretherton and Park (2009) improved the representation of marine stratocumulus-capped boundary layer in the community atmospheric model (CAM) with a set of new parameterizations including the introduction of a diagnostic TKE, diffusion on adiabatically conserved variables and cloud-top entrainment parameterization for convective layers.

This study tries to answer a current weakness of the turbulent scheme in ECHAM5-HAM: the cloud-top entrainment in stratocumulus clouds is not represented properly by the turbulent scheme of the current standard version with a coarse resolution. We thus implement an explicit cloud-top entrainment parameterization on top of stratocumulus clouds. In addition, we adapt the turbulent diffusion to be active on pseudo-adiabatic conserved variables (conserved under phase change), in the aim of using a more physical parameterization. This study is organized as follows: Section 2 briefly describes the actual boundary layer scheme. Section 3 describes the implementation of the explicit entrainment. In Sects. 4 and 5 we present the impact of the new parameterization on the model, first in a single column model (SCM) study and then on a global scale. Conclusions are presented in Sect. 6.

ACPD
11, 1971–2023, 2011

2 Description of the model ECHAM5-HAM

We use the Hamburg general circulation model (GCM) ECHAM5 (Roeckner et al., 2003) coupled to the double-moment modal aerosol microphysics scheme HAM (Stier et al., 2005). The cloud scheme in ECHAM5-HAM includes the double-moment cloud microphysics scheme for cloud droplets and ice crystals (Lohmann et al., 2007). In the 3-D simulations we use a climatological sea surface temperature and ice extend. The resolution used is T63 (grid box size of $1.875^{\circ} \times 1.875^{\circ}$) with 31 levels in the vertical and a time step of 12 min.

The turbulent scheme in the standard ECHAM5 model is described in Brinkop and Roeckner (1995). A brief summary of the various parameterizations relevant for the present study is given here. The turbulent fluxes of non-conserved variables (water vapor mixing ratio; liquid water mixing ratio, q_l; ice water mixing ratio, q_i; and dry static energy s, respectively) are expressed in terms of downgradient diffusion

$$\overline{w'\chi'} = -K_\chi \frac{\partial \bar{\chi}}{\partial z} \tag{1}$$

with $\chi = q_v, q_l, q_i$ and s. The eddy diffusivity K_χ follows an 1.5 order closure scheme (Prandtl-Kolmogorov parameterization), proportional to the square root of the TKE (e):

$$K_\chi = l S \sqrt{e} \tag{2}$$

where l is the mixing length (Blackadar, 1962) and S a stability correction. The implicit resolution of the resulting second order diffusion equation $\partial \bar{\chi}/\partial t = \partial \overline{w'\chi'}/\partial z$ is described in the appendix of Schulz et al. (2001). The eddy diffusivities for heat and moisture are assumed to be the same, i.e. $K_h = K_q$. ECHAM5 solves a prognostic equation for TKE containing an advective term, the buoyancy flux $g/\theta_v \overline{w'\theta_v'}$ (production or destruction of e by buoyancy, θ_v is the virtual potential temperature), shear stress, turbulent transport and dissipation, respectively. The buoyancy flux is expressed in terms of the following conserved variables: Liquid potential temperature ($\theta_l = \theta - \frac{L_v}{c_p}\frac{\theta}{T} q_l$, with

ACPD
11, 1971–2023, 2011

θ, T the potential resp. physical temperature, c_p the isobaric specific heat of air and L_v the latent heat for vaporization), total water content (q_t) and the interpolated cloud fraction σ_i on the interface levels:

$$\frac{g}{\theta_v}\overline{w'\theta'_v} = \frac{g}{\theta_v}\left(A\overline{w'\theta'_l} + D\theta\overline{w'q'_t}\right) = -K_h N^2 \quad (3)$$

$$A = \sigma_i A_s + (1-\sigma_i)A_u \quad (4)$$

$$D = \sigma_i D_s + (1-\sigma_i)D_u \quad (5)$$

with the subscript u (resp. s) describing the unsaturated (resp. saturated) contributions. The coefficients $A_{s,u}$ and $D_{s,u}$ are defined according to Deardorff (1980). The cloud fraction σ is calculated from the host model on the layer midpoints. σ_i is interpolated linearly with respect to the pressure on the interface layer. The buoyancy flux depends strongly on the cloud cover. N is the Brunt-Väisälä frequency.

3 Cloud-top entrainment in ECHAM5

Here we describe a new version of the boundary layer scheme in ECHAM5 which includes a parameterization of cloud-top entrainment in the stratocumulus regions. The different simulations are summarized in Table 1.

3.1 Diffusion on moist adiabatic conserved variables

To describe the turbulence in a more physical way we adapted the turbulent scheme to act on pseudo-adiabatic variables (conserved under phase change), i.e. total water mixing ratio q_t and moist static energy $s_l = c_p T + gz - L_v q_l - L_s q_i$ (where L_s is the latent heat of sublimation). For simplicity these variables are referred as moist conserved variables in the following. The turbulent diffusion of the conserved variables is equivalent to the diffusion being done on the standard variables because the operator $(\partial/\partial z)$ is linear. One could argue that it is not worth changing anything if the total amount

ACPD
11, 1971–2023, 2011

of diffused water remains identical. However, this is not completely true, because the complete system is non-linear. Indeed, the GCM computes a prognostic equation separately for each phase. Thus the mixing ratio profiles which enter the following physical routines will be different. For example the convection subroutine follows directly the turbulence subroutine and uses updated profiles. The incoming profiles will thus be different if the diffusion is done on moist conserved variables or on standard variables. Furthermore, in reality, the turbulence transports air parcels with a certain amount of total water and does not distinguish between phases. We thus improve the overall coherency and consistency of the model.

When the turbulent diffusion is applied to moist conserved variables, the tendencies for each standard variables due to diffusion are still needed by the model to compute the conservation equations independently for each phase. The problem is then to separate the condensate and the vapor tendencies from the total mixing ratio tendency and determine the temperature tendency from the diffused conserved variables. Depending on which cloud cover scheme is used, the cloud cover can provide additional information. In the relative humidity based cloud cover scheme by Sundqvist et al. (1989), the cloud cover is a diagnostic variable depending only on the water vapor mixing ratio and temperature. It cannot be used to get more information for determining how much of the total mixing ratio belongs to which phase. By using the simplest assumption, in which liquid water is not transported, it turns out that the condensation in the large-scale condensation routine associated with this cloud cover scheme tends to reach the same state based on the total mixing ratio and temperature, independent of which fration of total water mixing ratio is diffused as condensate. Thus, the impact of the diffusion on moist conserved variable is small when using the cloud cover scheme by Sundqvist et al. (1989).

On the other hand, the statistical cloud cover scheme by Tompkins (2002) carries a prognostic cloud cover which can give us one more information in order to disentangle the water vapor from the condensate (the ice/liquid fraction is supposed to be constant during diffusion). This cloud cover scheme uses a probability density function (PDF)

ACPD
11, 1971–2023, 2011

of total mixing ratio for the computation of the stratiform cloud cover. The PDF is described by a beta distribution $G(q_t)$, which is determined by four parameters. The integration of the PDF between the saturation mixing ratio (q_s) and infinity corresponds to the cloud fraction σ.

$$\sigma = \int_{q_s}^{\infty} G(q_t) dq_t . \quad (6)$$

Consequently, the liquid water mixing ratio is related to this integration by the relation

$$\overline{q_c} = \int_{q_s}^{\infty} (q_t - q_s) G(q_t) dq_t . \quad (7)$$

In ECHAM the parameters determining the PDF are: The skewness q (prognostic equation), a shape parameter (set constant for simplicity), the prognostically computed total mixing ratio q_t and condensate mixing ratio $\overline{q_c} = \overline{q_l} + \overline{q_i}$ (Tompkins, 2002). This system is not closed in case of overcasted or clear sky conditions ($\overline{q_c} = \overline{q_t}$, $\overline{q_c} = 0$). In these cases a prognostic variance equation (or more precisely, a prognostic equation for the width of the distribution ($b_t - a_t$), where a_t and b_t are the lower and upper bounds of the distribution) is solved. To separate the total mixing ratios tendencies for the different phases, the idea is to compute the water total mixing ratio, skewness and variance of the PDF only due to turbulent diffusion processes. The diffused PDF can then be reconstructed and the liquid water after diffusion can be diagnosed from the diffused PDF using Eq. (7).

This assumes that the PDF corresponds exactely to the condensate mixing ratio. By testing the accuracy of this method to determine the amount of condensate, we found that very often the skewness and width of the distribution do not correspond to the total, condensate and vapor mixing ratio. Figure 1 sketches what is happening in the model: In theory the shape of (and area under) the PDF corresponds to the mean grid-box variables (if one is known, the other can be deduced and conversely). But for stability

ACPD
11, 1971–2023, 2011

reasons, the PDF is not allowed to be too narrow, the threshold being $(b_t - a_t) \geq (C \cdot \overline{q_v})$. In cases where the computed width is artificially increased to be above the threshold, the described method leads to an artificial increase of the width $(b_t - a_t)$. Afterwards the width of the PDF does not necessarily correspond to the actual state of the grid cell anymore and $\overline{q_c}$ computed from Eq. (7) does not correspond to the actual amount of condensate in the grid box. In these cases the cloud cover, which is computed after the widening, is overestimated as compared to the actual amount of condensate. This widening does not cause any conservation problem in the standard model as the PDF is only used to compute the cloud cover. In the new presented version, the diffused condensate is aimed to be computed from the area under the diffused PDF. If the PDF is widened artificially, we can create or destroy water unphysically. In STD, the factor C is 10% (tunable parameter, A. Tompkins, personal communication). To be able to compute accurately the condensate from the PDF, we reduced it to $C = 0.1\%$. This lowers the frequency of the artificial widening, and when the distribution is widened, the associated error is largely reduced.

In order to determine the value of C, we proceeded as follow. We used the EPIC SCM experiment (Bretherton et al., 2004) where the observations of a warm cloud lasted for few days. We overwrite the temperature and water vapor mixing ratio profiles at each time step to have always idealized profiles. We computed the PDF from the total water and condensate water mixing ratio values for each grid-box as the cloud cover routine normally does, meaning applying the artificial widening. We then computed the values of liquid water mixing ratio corresponding to the widened PDF following Eq. (7). The results are shown in Fig. 2. The liquid water mixing ratio associated with the PDF is overestimated compared to the actual water liquid mixing ratio of the grid-box. The high errors occur almost always in overcasted conditions (not shown) because the variance is used to build the PDF only in overcasted or clear-sky conditions. The error is largest for C=10% as one can clearly see in Fig. 2. By reducing the threshold by a factor of 10 (C=1%) the overestimation decreases, but is still visible, particularly at low $\overline{q_c}$. We thus decided to reduce the threshold by a factor of 100 (C=0.1%), where the errors for

ACPD
11, 1971–2023, 2011

the EPIC campaign became insignificant. However the artificial widening can still occur with C=0.1% as can be seen in Fig. 2 in the zoom of the left panel. Therefore to ensure a conservation of the mixing ratios, we apply the algorithm that computes q_c twice in the turbulent routine: The first time at the beginning of the turbulent routine, and then at the end. The difference between these two values is the tendency associated to turbulence, that we are looking for.

Figure 3 shows the resulting total cloud cover averaged over three years of simulation after three months spin-up. For comparison, data from the International Satellite Cloud Climatology Project (ISCCP, Rossow and Schiffer, 1999) averaged over the period from 1983 to 2005 are displayed. Reducing the minimum of the distribution reduces the cloud cover, but does not affect directly the water condensate mixing ratio as the condensate is one of the variables determining the total mixing ratio PDF. In cases where the width of the PDF is smaller than 10% of $\overline{q_v}$, the microphysical scheme of RED sees a denser cloud than STD which precipitates more, diminishing in turn the LWP. The strong decrease in cloud cover in RED occurs almost everywhere. The strongest effect can be seen in subtropical regions, regions with boundary layer clouds where the distribution is more skewed. Indeed turbulence reduces the skewness of the PDF, tending toward a symmetric one (Tompkins, 2002). The reduction of C implies a very large change in the global cloud cover, and certainly affects the radiative budget. Thus every follow-up development is not in balance any more. We do not want to tune the model at this point, as the goal is to study the relative change due to the implementation of diffusion on moist conserved variables, RED is considered as the new reference run for MCV. In this context, the cloud coverage in all the stratocumulus regions has been significantly improved as we can see in Fig. 4 (left panel). One can see an increase of cloud cover everywhere between 30° S and 60° S, but RED underestimates clouds significantly in this region as compared to STD with a large increase in typical stratocumulus regions. We observed that the diffusion on moist conserved variables inverts the effects of RED (non-exhaustive list) and is similar to STD with respect to the following variables: ice mixing ratio, sensible and latent heat

ACPD
11, 1971–2023, 2011

flux, precipitation. In fact, MCV maintains a broader PDF as RED inside the cloud layer, so that, on average, the auto-conversion does not see a denser cloud as in the STD version. This means that often, MCV wideneth the distribution beyond the threshold of STD ($10\% \cdot \overline{q_v}$). So as shown in Fig. 4, the cloud cover in MCV is restored to its STD state thanks to a more physical representation.

Finally, the reduction of the minimal width of the PDF followed by the diffusion on moist conserved variables is useful, as it decreases the impact of the tuning parameter (C) by using a more physical turbulent diffusion. This version with diffusion on moist conserved variables and reduced minimal width of the distribution (MCV) is considered as a new reference version in the following.

3.2 Regions of entrainment occurrence

The entrainment at the top of PBL is particularly important as it regulates the PBL's properties. A difficult question is where and at which level to apply the PBL top explicit entrainment. The natural answer is at the top of the PBL. Unfortunately, the PBL top is not readily found in a GCM due to the low resolution. A criterion based on the difference of the dry static energy with its ground value and the friction velocity is implemented in the standard PBL scheme of ECHAM5; but this is not really accurate. Typically a criterion based on the Richardson number threshold (e.g., Grenier and Bretherton, 2001) is used to detect the PBL top. This criterion sometimes predicts PBL top at the cloud base in ECHAM5, probably due to a local stabilization at cloud base due to latent heat release. Thus we define a "stratocumulus criterion", which consists of different requirements. We want to exclude shallow cumulus regions for several reasons. First, a cloud-top entrainment parameterization is already included in the new shallow cumulus routine of von Salzen and McFarlane (2002), further developed and implemented by Isotta et al. (2010). The latter parameterization will be coupled to the explicit cloud-top entrainment presented in this study in the future. Second, the importance of cloud-top entrainment in those clouds is still a matter of debate. Using LES simulations of shallow cumuli clouds, Heus et al. (2008) studied the source of entrained air within

ACPD
11, 1971–2023, 2011

the cloud. Whereas one of the method used could indicate some cloud-top mixing, the Lagrangian particle tracking shows that virtually all the mixing comes from lateral entrainment. Third, the entrainment parameterization was developed from stratocumulus region observations. This parameterization would simulate very high entrainment rates in shallow cumulus regions. Indeed, de Roode et al. (2006) showed that most of the known parameterizations tend to increase to infinity for a decreasing temperature jump if the other properties remain unchanged. For these reasons, we decided to activate cloud-top entrainment only in regions of stratocumulus clouds. The cloud-top entrainment parameterization is thus applied on grid points with the following properties: A cloud is present, the subsidence is positive, the pressure of the cloud top (considered as top of PBL) is below 700 hPa and the low tropospheric stability (LTS) exceeds 20 K. The LTS is defined as the difference between the potential temperature θ at 700 hPa and at the ground. This threshold is based on the climatology of low-level clouds developed by Klein and Hartmann (1993). In Fig. 5 the annual frequency of occurrence of these criteria for stratocumulus top in the standard ECHAM5-HAM is shown. This criterion is most frequently met in tropical stratocumulus regions. One can see that it is met at most 50% of the time. The most restrictive part of this criterion is that a cloud needs to be present.

A disadvantage of this criterion is that it does not allow an explicit entrainment at the top of the dry convective boundary layer where entrainment is effective and very important as well. Moreover, it has not yet been demonstrated that the observationally derived LTS–cloud cover relationship will hold in a warmed climate. On the other hand, with this criterion, we ensure to compute the entrainment at the cloud top and thus at locations where the parameterizations was derived for. Furthermore, ECHAM5-HAM already computes a flux at the top of the PBL with the TKE scheme which will be used for dry convective boundary layer. Finally the observations of entrainment rates show values one order of magnitude higher when a cloud is present (Nicholls and Leighton, 1986; Nicholls and Turton, 1986).

ACPD
11, 1971–2023, 2011

3.3 Eddy diffusivity in cloudy/clear sky case

Because the criterion for the onset of the explicit entrainment closure depends on cloud cover, a clear sky would be treated differently if it were in a partially cloudy grid-box or in a totally clear-sky grid-box if we would apply a mean explicit entrainment above cloudy grid-boxes. Cheinet and Teixeira (2003) obtained more realistic PBL clouds by dividing the grid-boxes into two regions, i.e. cloudy and clear air. For each region, they compute a prognostic TKE and the derived eddy diffusivities are then averaged. Similarly, our approach is to divide the grid-box in a cloudy region (subscript c) and a clear region (subscript e) but averages the different fluxes instead of the eddy diffusivities.

In ECHAM the cloud is assumed to occupy the whole vertical layer, so the upper interface of a cloudy grid-box is exactly the cloud top. If the stratocumulus criterion is fulfilled, the fluxes of total mixing ratio and moist static energy at the interface of the grid-boxes are averaged using the cloud cover σ at the layer midpoint ($\chi = q_t, s_l$):

$$\begin{aligned}\overline{w'\chi'} &= \sigma\,\overline{w'\chi'}^{c} + (1-\sigma)\,\overline{w'\chi'}^{e} \\ &= -\left(\sigma K_h^{c}\frac{\partial\overline{\chi}^{c}}{\partial z} + (1-\sigma)K_h^{e}\frac{\partial\overline{\chi}^{e}}{\partial z}\right). \end{aligned} \tag{8}$$

We do not want to deeply affect the PBL turbulent diffusion scheme, thus the same structure and numerical algorithm which is already implemented has been kept. We then transform the Eq. (8) to be solved directly by the host turbulent solver. The fluxes are supposed to be proportional to the gradient of the mean quantity with an "equivalent" eddy diffusivity K_χ^{eq}:

$$\overline{w'\chi'} = -K_\chi^{eq}\frac{\partial\overline{\chi}}{\partial z} \tag{9}$$

where $\overline{\chi}$ is the mean value for the grid-box $\overline{\chi} = \sigma\,\overline{\chi}^{c} + (1-\sigma)\,\overline{\chi}^{e}$. The variable $\overline{\chi}^{c}$ is computed assuming the cloud being exactly at saturation with all the liquid water being inside the cloud. Thus,

ACPD
11, 1971–2023, 2011

$$\overline{q}_{\mathrm{t}}^{\mathrm{c}} = q_{\mathrm{sat}}(T) + \overline{q}_{\mathrm{l}}/\sigma, \quad \overline{q}_{\mathrm{t}}^{\mathrm{e}} = \frac{\overline{q}_v - \sigma q_{\mathrm{sat}}(T)}{1-\sigma} \tag{10}$$

$$\overline{s}_{\mathrm{l}}^{\mathrm{c}} = c_p T - gz + \overline{q}_{\mathrm{l}}/\sigma, \quad \overline{s}_{\mathrm{l}}^{\mathrm{e}} = c_p T - gz. \tag{11}$$

χ in the grid-box above the cloudy layer is supposed to be completely homogeneous so the profiles in the clear and cloudy part differ only in the cloudy part of the grid-box. If we discretize and exclude the case of vanishing gradients of the mean quantities, we obtain

$$K_\chi^{\mathrm{eq}} = \sigma K_{\mathrm{h}}^{\mathrm{c}} \frac{\Delta\overline{\chi}^{\mathrm{c}}}{\Delta\overline{\chi}} + (1-\sigma) K_{\mathrm{h}}^{\mathrm{e}} \frac{\Delta\overline{\chi}^{\mathrm{e}}}{\Delta\overline{\chi}}. \tag{12}$$

K_χ^{eq} is not a physically interpretable quantity. It is the equivalent eddy diffusivity which would transport the same amount of matter as the weighted two fluxes, in a first order turbulence closure. It depends strongly on the mean gradient, for example if the mean gradient is very small, K_χ^{eq} can become very large to compensate. The quantity which is conserved is the mean flux $\overline{w'\chi'}$ of the quantity χ.

This method presents an advantage over the method by Cheinet and Teixeira (2003) as it allows the representation of fluxes of opposite direction at the top of the clear and the cloudy part of the grid-box. This situation is shown schematically in Fig. 6. The gradient of χ is negative above the cloudy region but positive above the clear region. By looking separately at each sub-box, the turbulent transport is positive above the cloud, and negative above the clear part. The total flux of the box is the weighted average of both fluxes. The case when K^{eq} is negative is excluded in our simulations. This would mean that the turbulent transport flows in the opposite direction as the gradient of the mean variable. Since the surface scheme uses indirectly the eddy diffusivities and cannot properly handle a negative eddy diffusivity, these are excluded. Nevertheless, this situation rarely occurs. The case where the gradient of the mean variable is zero is also excluded. In a local 1 or 1.5 order closure, the flux associated to a vanishing

ACPD
11, 1971–2023, 2011

gradient is zero. If we wanted to take into account the case where the gradient of the mean variables is zero, while the gradient of the variables over both cloudy and clear environment are not zero, a more elaborate implementation would need to be considered. As the equivalent eddy diffusivity now depends on the gradient of the diffused quantity, we use a different K_χ^{eq} for heat and moisture, i.e. $K_q^{eq} \neq K_h^{eq}$ resulting from our new scheme.

The eddy diffusivity for the clear environment K_h^e is computed in the same way as the clear-sky grid-boxes, following Eq. (2) with a newly computed mixing length and stability function explicitly computed for the clear-sky part. The eddy diffusivity for the cloud top K_h^c is computed with the explicit entrainment parameterization:

$$K_h^c = K_q^c = w_e \Delta z. \tag{13}$$

where w_e is the entrainment velocity, the operator $\Delta\psi$ represents the jump of ψ over the entrainment zone (between grid points next to the top interface of the cloudy grid-box) and z is the height.

3.4 Entrainment parameterization

Several cloud-top entrainment parameterizations which can be based on sets of LES simulations (Lock, 1998; Moeng, 2000), theoretical considerations and fits to in-situ observations (Turton and Nicholls, 1987) exist. Stevens (2002) examined several of these parameterization and concluded that the different parameterized rates can differ substantially. We choose to use the Turton and Nicholls (1987) entrainment closure for two reasons. First it is simple, it does not depend to much on the evaporative enhancement or TKE value. Second Sandu et al. (2009), who tested several entrainment parameterizations against LES data, found the smallest bias with this one. Thus, at the top of the stratocumulus-capped boundary layer, the entrainment velocity w_e is expressed as:

$$w_e = a \frac{w_\star^3}{z_i \Delta b^c}. \tag{14}$$

ACPD
11, 1971–2023, 2011

It is inversely proportional to the height of the boundary layer z_i and the buoyancy jump Δb^c over the entrainment zone. The subscript i represents the interface above the cloudy grid-box (z_i =height of the PBL)

$$\Delta b^c = \frac{g}{\theta_{v,i}} \left(\theta_{v,i-1/2} - \theta^c_{v,i+1/2} \right). \tag{15}$$

The convective velocity $w_\star$ is defined as proposed by Deardorff (1976):

$$w_\star = \left(2.5 \frac{g}{\theta_v} \int_0^{z_i} \overline{w' \theta'_v} \right)^{1/3}. \tag{16}$$

For the discretization of $w_\star$, we follow Bretherton and Park (2009).

The buoyancy flux at the top of the cloud layer follows Eq. (3):

$$\frac{g}{\theta_v} \overline{w' \theta'_v}^c = \frac{g}{\theta_v} \left(-w_e \left(A^c \Delta \theta^c_l + D^c \theta \Delta \overline{q_t}^c \right) \right) \tag{17}$$

It is not so clear which coefficients to use for A^c and D^c. The (sub-)saturated coefficients were computed from perturbation computations inside a (sub-)saturated medium. Assuming the cloud top to be wavy, we suppose the buoyancy flux to be half "saturated" and half "sub-saturated": $A^c, D^c = \frac{1}{2} A^c_s + \frac{1}{2} A^c_u$, same for D^c. The coefficients A^c_s, A^c_u, D^c_s and D^c_u are using the in-cloud values.

The entrainment efficiency $a = a_1(1 + a_2 E)$ in Eq. (14) simulates the enhancement of entrainment due to evaporative cooling of mixtures of cloudy and above-cloud air. We use the value $a_1 = 0.2$ as proposed by Turton and Nicholls (1987). The value of the constant a_2 is still a matter of discussion; we follow Bretherton and Park (2009) with $a_2 = 15$. The evaporative enhancement term is derived from Stevens (2002) and adapted to be coherent with our turbulent scheme:

$$E = \frac{g \overline{q_l}^c \beta_l}{\delta_d b^c - \delta_m b^c} \left(1 - \frac{\delta_m b^c}{\Delta b^c} \right)$$

ACPD
11, 1971–2023, 2011

with

$$\beta_\mathrm{l} = \frac{1}{\theta_\mathrm{v}}\left(\frac{L_\mathrm{v}}{c_p}\left(1+\epsilon\overline{q_\mathrm{t}}^\mathrm{c}\right) - T(1+\epsilon)\right)\left(\frac{p_0}{p}\right)^{R_\mathrm{d}/c_p},$$

and the buoyancy perturbation one would expect in case of sub-saturated or saturated processes ($\delta_\mathrm{d}b^\mathrm{c}$ and $\delta_\mathrm{m}b^\mathrm{c}$) if the layers would have the same energy and total mixing ratio.

$$\delta_\mathrm{d}b^\mathrm{c} = \frac{g}{\theta_\mathrm{v}}\left(A_\mathrm{u}\Delta\theta_\mathrm{l}^\mathrm{c} + D_\mathrm{u}\theta\Delta\overline{q_\mathrm{t}}^\mathrm{c}\right)$$

$$\delta_\mathrm{m}b^\mathrm{c} = \frac{g}{\theta_\mathrm{v}}\left(A_\mathrm{s}\Delta\theta_\mathrm{l}^\mathrm{c} + D_\mathrm{s}\theta\Delta\overline{q_\mathrm{t}}^\mathrm{c}\right),$$

p (p_0) is the pressure (reference pressure, $p_0 = 1000\,\mathrm{hPa}$), R_d and R_v the gas constants for dry air and water vapor, respectively, and $\epsilon = (R_\mathrm{d}/R_\mathrm{v})^{-1} - 1 = 0.608$.

3.5 Buoyancy production

Thus if the stratocumulus (Sc) criterion (presented in Sect. 3.2) is fulfilled, the buoyancy flux (which is a source term in the TKE conservation equation) is averaged the same way as for the other fluxes (Eq. 8) plus a contribution from the longwave radiation divergence:

$$\frac{g}{\theta_\mathrm{v}}\overline{w'\theta_\mathrm{v}'} = \begin{cases} \frac{g}{\theta_\mathrm{v}}\left(\sigma\overline{w'\theta_\mathrm{v}'}^\mathrm{c} + (1-\sigma)\overline{w'\theta_\mathrm{v}'}^\mathrm{e}\right) + \frac{g}{\theta_\mathrm{v}}A^\mathrm{c}\alpha\frac{1}{\rho c_p}\Delta F_\mathrm{rad} & \text{if Sc are present,} \\ \overline{w'\theta_\mathrm{v}'}^\mathrm{STD} + \frac{g}{\theta_\mathrm{v}}A\alpha\frac{1}{\rho c_p}\Delta F_\mathrm{rad} & \text{else.} \end{cases} \quad (18)$$

The buoyancy fluxes $\overline{w'\theta_\mathrm{v}'}^\mathrm{c}$ and $\overline{w'\theta_\mathrm{v}'}^\mathrm{STD}$ are expressed following Eq. (3). $\overline{w'\theta_\mathrm{v}'}^\mathrm{STD}$ uses the standard coefficients A and D defined in Eqs. (4)–(5) based on mean grid-box values. For the clear-sky environment buoyancy flux $\overline{w'\theta_\mathrm{v}'}^\mathrm{e}$, the coefficients are unsaturated $A^\mathrm{e} = A_\mathrm{u}^\mathrm{e}$, $D^e = D_\mathrm{u}^\mathrm{e}$ and are based on the clear-sky variables. $\overline{w'\theta_\mathrm{v}'}^\mathrm{c}$ is computed as described in Eq (17). The radiative term $\Delta F_\mathrm{rad}/\rho c_p$ is the radiative flux divergence

ACPD
11, 1971–2023, 2011

at the interface in temperature flux units ($K\,m\,s^{-1}$). The shortwave contribution is not taken into account because it is too diffuse and represents a very small contribution as compared to the longwave contribution (Deardorff, 1976). α represents the fraction of cloud-top radiative divergence occurring inside the discontinuous inversion. The value of the fraction is not known. Since Deardorff (1976) obtained good results with $\alpha = 0.5$, we use the same. The radiative fluxes were taken from the host model.

As radiative cooling occurs at the cloud top of all clouds, the radiative contribution in the buoyancy production is applied above all clouds, irrespective to the criterion presented in Sect. 3.2. Indeed, the radiative cooling is always part of the buoyancy production flux in the TKE equation. One could argue that the radiative cooling is already taken into account as the associated tendency enters the prognostic temperature prognostic equation. However, it does not properly enter the buoyancy production as it applies a constant cooling rate for the whole vertical gridbox. Thus the radiative cooling rate in the standard version has no destabilization effect on the cloud top because it does not change the lapse rate locally.

4 Results – single column model

The new version with an explicit cloud-top entrainment parameterization above stratocumulus described in the previous sections is called simulation ENTR (cf. Table 1).

4.1 Diurnal cycle and mean nocturnal profiles

The simulations are based on idealized observations taken during the second flight (A209) of the ASTEX Lagrangian Experiment campaign, which took place near the Azores in June 1992 (Albrecht et al., 1995). The observations during this night flight reported stratocumulus with a lot of drizzle (de Roode and Duynkerke, 1997). The initial profiles are based on the GCSS stratocumulus modeling intercomparison case set up by Duynkerke (1996). The boundary layer has a uniform liquid potential temperature

ACPD
11, 1971–2023, 2011

of θ_l =288 K, and a total mixing ratio of q_t =10.2 g kg^{-1}. The jumps across the inversion are 5.5 K and −1.1 g kg^{-1}, respectively. The simulations are conducted with a constant surface temperature of 290.8 K. We choose to simulate this intercomparison and not the referenced modeling intercomparison based on the third flight (RF06) (Duynkerke et al., 1999) because during the latter flight, a transition case with shallow cumuli growing under stratocumulus deck was observed. The aim here is not to look at the transition from stratocumulus to trade cumulus, but to qualitatively examine the diurnal cycle of a quasi-equilibrium stratocumulus case.

Figures 7 and 8 show the time dependence of TKE, cloud cover and q_l. In the standard (STD) version, there is no diurnal cycle in the cloud cover because the boundary layer is very moist and the grid-box is always saturated. q_l has a small diurnal cycle (Fig. 8). TKE shows a strong diurnal cycle, with very high values at cloud base. In MCV, one can observe a more pronounced diurnal cycle than in the STD version. Lastly, the diurnal cycle in cloud cover is even more pronounced in the ENTR version.

In the STD simulation of Fig. 7, there is a spin-up of about one day, where no TKE is present. The STD version has unrealistically high values of TKE (up to 1.35 m^2 s^{-2}), clearly out of the range of observations (between 0.1 and 0.5 m^2 s^{-2} according to de Roode and Duynkerke, 1997). The high values of TKE follow a diurnal cycle due to radiative heating/cooling. During the night the cloud is cooled by longwave radiative cooling, it destabilizes the profile at cloud base (instead of at cloud top). This induces a strong buoyancy production at cloud base. The highest values of TKE in STD occur in a narrow time interval before midnight, the latent heating of condensation counteracting the destabilization due to radiative cooling. These processes show their effect at cloud base, because in a coarse resolution like the one we are using, the cloud occupies only one model layer and so the radiative cooling and induced condensation act in the middle of the cloud instead of at the cloud top as they should.

In the MCV experiment, the diurnal cycle of the TKE is still seen at the cloud base, but the TKE values are more reasonable. This stems from the smaller values of q_l, which induce a smaller radiative cooling contribution. The time evolution of the cloud

ACPD
11, 1971–2023, 2011

cover exhibits a diurnal cycle: q_l is smaller (all the liquid water is rained out during the first hour of simulation), thus the shortwave radiation is able to evaporate sufficient q_l to have an impact on the cloud cover. The TKE increases and decreases smoother in the MCV than in STD simulation at the cloud base. This is due to the smaller radiative cooling which prevents the gradient of virtual potential temperature to jump suddenly from being positive in one time step to negative in the next time step.

In the ENTR simulation, one can see the maximum of the TKE at the top of the cloud due to the radiative contribution in the buoyancy production, more representative of a typical stratocumulus. TKE is more in the range of measurements than in STD and TKE is more constant during the night than in the other simulations. A more pronounced diurnal cycle can be seen in the cloud cover or equivalently in q_l than in MCV. In general, ENTR better represents the observed features of a typical stratocumulus (e.g., Hignett, 1991; Bretherton et al., 2004), namely that during the night the cloud thickens and cloud top rises. The latter does not happen in ECHAM due to the coarse vertical resolution. The strong radiative cooling drives the turbulence, trying to mix the PBL during the night and triggering a higher entrainment rate as can be seen in Fig. 9. q_l is smaller because the entrainment dries and warms up the PBL from the top.

Figure 9 shows the time-serie of the simulated entrainment velocity. The values are quite low. As expected, the entrainment increases during night in response to the turbulence increase. The strange behavior of the first simulated day should be taken with care, as they occur during the spin-up time. However, the whole time-serie seems physical.

Figure 10 shows the LWP and precipitation for these three simulations. They all reach a certain equilibrium, with a higher LWP during night inducing more precipitation. The values are smaller in MCV than in STD because of higher precipitation during the first hours of simulation. Looking at the LWP and precipitation at the ground, one could be tempted to extrapolate and say that all simulations are reaching the same equilibrium after some days of simulations. However, this is not the case (not shown). The lower panels of Fig. 10 show the sensible and latent heat flux. Again, the PBL is

ACPD
11, 1971–2023, 2011

warmer in the ENTR simulation inducing a smaller sensible heat flux (SH). The latent heat flux (LH) does not experience a diurnal cycle any more in ENTR, indicating that the vapor mixing ratio at the first level remains relatively constant. Thus, the eddies are not reaching the ground. This is probably due to the small values of TKE in the middle of the PBL, between PBL top and the surface as can be seen in Fig. 11. This may be indicative of a problem in the turbulent transport of TKE. However, the turbulent transport of TKE is proportional to TKE, so a small TKE implies a small turbulent transport of TKE.

The effect of the new parameterizations on the mean night profiles of the first night after the spin-up for the ASTEX simulation is presented in Fig. 11. The influence of the new parameterization on the liquid potential temperature θ_l and on q_t is small. The zooms show that MCV is less well-mixed and more stable at the base of the cloud, because of smaller TKE values. The θ_l profile of ENTR is also more stable because of the warming of the cloud top due to entrainment. The buoyancy production at cloud base becomes a sink, because of the warmer cloud. There is less liquid water in ENTR than in MCV and less in MCV than in STD. The TKE profiles correspond to this phenomenon: In STD and MCV, the cloud layer is colder with respect to the sub-cloud layer because of the radiative cooling. The stability at cloud base becomes smaller (or negative). The upcoming buyancy flux, which is a source of TKE, increases. Thus, they have a large TKE at the base of the cloud due to radiative cooling. ENTR has the peak of TKE and the buoyancy production at the top of the cloud due to the explicit radiative cooling in the buoyancy production. Even if the buoyancy production is negative in MCV at the base of the cloud, it is less negative than during the day. This allows the shear stress to produce more TKE. Because of the coarse resolution, the fine structure of positive buoyancy production due to radiative cooling just below negative buoyancy production due to entrainment as obtained with LES simulations (Lenderink and Holtslag, 2000) cannot be resolved. Thus, the buoyancy flux at the top of the cloud in ENTR represents both the negative contribution from entrainment and the positive contribution from radiative cooling. The radiative cooling contribution

ACPD
11, 1971–2023, 2011

seems to dominate very often in the SCM. As a sensitivity study, the same simulation was conducted with the fraction of LW cooling acting on buoyancy production reduced to $\alpha = 0.1$ to compare with the previous simulation where $\alpha = 0.5$. This simulation is included in Fig. 11. The results are reasonable. The TKE maximum at the cloud top is smaller, and q_l is a little larger. The latter phenomenon can be explained by the fact that the buoyancy production at cloud top enters in the computation of the entrainment rate by the way of the convective velocity. So a smaller radiative contribution will yield a smaller entrainment rate (as seen on Fig. 9) and less drying. The time dependence of the simulation with $\alpha = 0.1$ is similar to the standard ENTR version displayed in Fig. 7 (not shown), but the entrainment rate is even smaller.

We try to compare the profiles of the first night with the measurements obtained during the second flight of the ASTEX campaign on Fig. 11. The observations of buoyancy production and TKE from de Roode and Duynkerke (1997) are also shown in Fig. 11 (circles) as well as the top and base of the observed cloud (dashed gray horizontal lines). The cloud is at higher altitudes than the observations, as can be seen in Fig. 7; the cloud rises in the beginning of the simulation due to an onset of convection. Concerning the TKE, the simulated values at cloud top have similar values as the observed. However, the observed profile shows a rather constant profile of TKE in the PBL. The STD version is the only one where TKE is better distributed in the vertical because the profiles are less stable, so there is more TKE production by buoyancy. Again, there is could be a problem of TKE transport inside the PBL.

During the SCM experiment with the ENTR version, the mean entrainment velocity at the top of the highest cloud over the four days is $0.5\,\mathrm{mm\,s^{-1}}$ and $0.1\,\mathrm{mm\,s^{-1}}$ for $\alpha = 0.5$ and $\alpha = 0.1$, respectively. This is one to two orders of magnitude smaller then the averaged entrainment velocity over the four flights of the ASTEX campaign that were measured to be $9\pm5\,\mathrm{mm\,s^{-1}}$. Moreover, the different computations of the entrainment rate during other field campaigns obtained similar values: $2\,\mathrm{mm\,s^{-1}}$ during the night and very small during day (Duynkerke and Hignett, 1993) or $3.8\pm1\,\mathrm{mm\,s^{-1}}$ during the night flight RF01 of the DYCOMS-II campaign (Stevens et al., 2003). The entrainment

ACPD
11, 1971–2023, 2011

closure is proportional to the convective velocity, the latter depending on the simulated TKE. The parameterized entrainment velocities are low partly because the TKE values inside the boundary layer in the ENTR SCM version are low. However, we think that it is safer having an entrainment rate that is too small than the opposite in order to deviate as little as possible from the standard model and to preserve the inversion.

The buoyancy production profile in the ENTR version is more what is expected in typical nocturnal well mixed stratocumulus. The buoyancy flux increases with height inside the cloud (e.g., Deardorff, 1976) and follows better the measured profile, with the maximum near the top of the cloud, and not at its base.

4.2 Influence of aerosols on the liquid water path

After having investigated the effect of the new parameterization on vertical profiles, we wanted to see if we can qualitatively reproduce the LES results of Ackermann et al. (2004) with the SCM experiment based on ASTEX. By increasing the cloud droplet number concentration (CDNC) in different nocturnal stratocumulus simulations, Ackermann et al. (2004) obtained a decrease of precipitation and an increase in the entrainment rate. The LWP was increasing or decreasing depending on the relative humidity of the free troposphere above the cloud. The comparison with the different simulations presented here can only be qualitative. Indeed, the entrainment closure (Eq. 14) does not depend explicitely on CDNC. w_e can only increase indirectly because of the increase of the liquid water mixing ratio inside the cloud. Thus, it is not possible to simulate a decreasing LWP for increasing CDNC with this parameterization. The aim is to see if the dependence of the LWP to CDNC is reduced.

Figure 12 shows a sensitivity study of the LWP, precipitation and entrainment rates averaged over the second hour of simulation as a function of the CDNC. The second hour of simulation was chosen because changing the CDNC affects all the model dynamics. Indeed, the change in precipitation rate and radiative budget then imply lots of feedbacks so that the different experiments are not in a similar state anymore. They can no longer be compared with each other in a meaningful way. Thus one needs to

ACPD
11, 1971–2023, 2011

consider Fig. 12 with care, as we are still in the spin-up period. However, as can be seen in Fig. 9, the entrainment velocity has comparable values during the second hour of simulation as during the second night.

Figure 12 is encouraging in the sense that with the ENTR parameterization, we obtain a reduction of the dependence of LWP with CDNC in ENTR compared to MCV. The entrainment closure does not depend explicitly on CDNC, but on the total water jump across the inversion. The entrainment rate does not increase directly due to the increase of droplet number, but because of the increase of LWP due to the increase in CDNC. The entrainment parameterization reduces more LWP for large CDNC values than for small CDNC values. The entrainment values are quite small, as discussed in the precedent section.

5 Results – global simulations

5.1 General boundary layer structure

To have a better idea of the vertical structure of the boundary layer in a stratocumulus region, we extract the California stratocumulus region as the area between 20° N–30° N and 120° W–130° W, as defined by Klein and Hartmann (1993). The average summer season (June, July, August, JJA) profiles over five years are shown in Fig. 13. The PBL in ENTR is clearly drier (but the free atmosphere above the inversion contains more vapor) and is a little bit warmer than the one of MCV. Thus the liquid mixing ratio and the cloud cover are reduced.

PBL top entrainment transforms the laminar air from above the PBL inside the PBL and lets the PBL grow. Because of the coarse resolution, the effect of the parameterization is to exchange air masses between the first free tropospheric level and the PBL top, this reduces the inversion strength, as we can see on the mean profiles in Fig. 13. Indeed, if we look at the inversion on top of the PBL, the profiles of θ_l and q_t simulated by ENTR are worse than those simulated with MCV. We plan to implement

ACPD
11, 1971–2023, 2011

a local increase in resolution to better represent the inversion. On the other hand, one can see a small increase of the PBL height in ENTR.

The effect of smoothing the TKE in simulation ENTR that we saw in the ASTEX simulations can be seen here as well. The mean TKE profile in ENTR has smaller values than the one in MCV. The latter has unrealistically high values, whereas the values of TKE are in the right have a better order of magnitude in ENTR.

5.2 Pacific cross-section

During the GCSS/WGNE Pacific cross-section intercomparison (Teixeira et al., 2009), ECHAM5 showed a very shallow layer of upward vertical motion in the intertropical convergence zone (ITCZ), with insufficient cloud cover. Over the ITCZ, the layer of upward mean vertical velocity did not extend above 700 hPa. Moreover, the cloud cover was too close to the surface in the stratocumulus regions (Teixeira et al., 2009). Here the same boundary conditions are used but for JJA 2000, with climatological sea surface temperature. We are looking at the simulations along a Pacific Ocean cross-section, from the stratocumulus region off the coast of California (35° N, 125° W), to the deep convection region (1° S, 173° W), over JJA 2000. Figure 14 shows the cross-section simulated with the different versions. For comparison, the corresponding pictures of the ECMWF Re-Analysis ERA40 (Uppala et al., 2005) and ERA-Interim (Simmons et al., 2006) are also displayed in the lower rows. ERA-40 data underestimate the cloud cover in the stratocumulus regions and overestimate it in the ITCZ (Teixeira et al., 2009), while ERA-Interim shows an improvement for stratocumuli and clouds in general (Köhler, 2005). The hydrological cycle is improved in terms of the precipitation in ERA-Interim (Simmons et al., 2006), but an improvement in the Hadley circulation has not been demonstrated. For this reason, both ERA40 and ERA-Interim are displayed and we are taking the observations of subsidence as equally likely. The observational data are averaged only from 12-hourly data to be fully comparable with the model output.

ACPD
11, 1971–2023, 2011

In general, all the versions produce realistic cross-sections. We simulate a rising inversion towards the equator that marks the transition from stratocumulus to deep convection. The new parameterization changes the different patterns of cloud cover, relative humidity and subsidence. First, the cloud coverage in shallow cumulus regions from STD to MCV is reduced, the PBL is drier. But on the other hand, the cloud cover is increased in the stratocumulus regions (latitudes 32° N–35° N), probably because the turbulent diffusion does not try to reduce q_l anymore. It is interesting to see that MCV has less high level cirrus in the stratocumulus regions, in better agreement with observations. Since there is no snow falling in the cross-section in any of the versions, it is probably due to the reduction of the vertical velocity in the tropical region which transports less vapor in the upper layers.

Comparing MCV and ENTR, one can see some improvements. First, ENTR produces fewer clouds in the stratocumulus region than MCV. This is a direct effect of the explicit entrainment which dries and warms the PBL in these regions. The transition from stratocumulus to deep convection (between about 10° N to 30° N) is better in the ENTR version than in MCV, in terms of cloud cover. There are more clouds, which has a strong effect on the outgoing radiation. At first, it might seem surprising to have a strong effect in this region, as the explicit entrainment is not active there. The TKE contribution is present every time when there is a cloud. So if there is a cloud, the source of TKE at the top of clouds eventually induces a better mixing across the layer, drying and warming the surface layer. This induces a higher latent heat flux (LH) (and smaller sensible heat flux (SH)) at the surface as shown in Fig. 15. The convection scheme in all simulations is the Tiedtke (1989) scheme, where the closure to trigger shallow convection is strongly dependent on the surface evaporation. This higher latent heat flux triggers convection more frequently, which produces more clouds. The higher LH results, on average, in a PBL with a higher vapor mixing ratio. At the surface, the vapor is transported higher up, causing the surface layer to be drier in ENTR than in MCV. The PBL then has a smaller relative humidity in ENTR, being a consequence of the drier and warmer surface layer. This is more comparable to ERA-Interim. It seems

ACPD
11, 1971–2023, 2011

that overall, the whole Hadley circulation seems to be reinforced, because of the increased convection: The updraft in the ITCZ penetrates higher up, and the descending subsidence is stronger. The 80% RH contour line is higher up in the ITCZ because of the higher vertical velocity. Nevertheless, if the increase in shallow cumuli shows up in each of five years climatological simulations on the cross-section, the enhancement of the Hadley circulation is not persistent. However, an enhancement in shallow convective activity does not necessary lead to an increase in the intensity of the Hadley circulation. For example Tiedtke et al. (1988) showed a higher intensity with more shallow convection, while von Salzen et al. (2005) did not. It could be more complicated as suggests Neggers et al. (2007), an increase of shallow convection also results in more intense convection but within a narrower area in the oceanic ITCZ.

Above the PBL in the stratocumulus regions (32° N–35° N), the free troposphere is colder and moister because of the enhanced exchange between the free troposphere and the PBL caused by more entrainment. Thus the relative humidity in this region is higher in the free troposphere (between roughly 600 and 800 hPa). Moreover the cloud base in ENTR is further away from the surface than in MCV. During the GCSS/WGNE Pacific Cross-section intercomparison (Teixeira et al., 2009), the simulated stratocumulus clouds were too close to the surface. However this could just be an artifact of the interpolation procedure as the cloud amount is smaller. As a result from the increased entrainment, the PBL top is higher and the relative humidity (RH) is smaller in the stratocumulus regions in simulation ENTR.

The area of smaller RH in MCV increases above the shallow cumulus regions (about 17° N and 500 hPa) is not present in ENTR anymore, because the vapor mixing ratio increases a bit, probably because there is more transport of moisture by the convection scheme higher up. However, RH is very sensitive to both absolute moisture and temperature. One can see that there is more precipitation in ENTR than in MCV in the ITCZ, which is a direct consequence of the enhanced convection.

ACPD
11, 1971–2023, 2011

5.3 Global distribution of cloud cover

The global distribution of cloud cover averaged over three years from simulation ENTR is displayed in Fig. 3 and the difference to MCV in Fig. 4. Overall, ECHAM misses the low-level clouds. The introduction of entrainment makes it even worse in the stratocumulus regions, it dries and warms these regions on average. On the other hand, one can see the increase in cloud cover in shallow cumulus regions in simulation ENTR because of the higher LH (not shown) inducing more convection (process described in Sect. 5.2). One can see a small increase in cloud cover over China going from MCV to ENTR. This corresponds to an increase in the frequency of the clouds in these regions, not to an increase in the cloud cover when there is a cloud present. It may be due to the modification of the triggering of the convection.

6 Conclusions

We implemented the explicit entrainment closure of Turton and Nicholls (1987) in the climate model ECHAM5-HAM. First, the diffusion is adapted to be performed on the pseudo-adiabatic conserved variables (conserved under phase change) θ_l (liquid potential temperature) and q_t (total mixing ratio). With the statistical cloud cover scheme by Tompkins (2002), we have to reduce the minimal width of the distribution of total mixing ratio for consistency. This has the effect that the microphysical scheme sees denser clouds which precipitate a lot, destroying the cloud cover. It affects greatly several quantities like precipitation and surface fluxes due to a warming of the surface layer. Diffusing the moist conserved variables (MCV) increases the cloud cover, as the water liquid mixing ratio is not diffused unphysically as in STD, and broadens the distribution. This re-establishes some of the affected global mean values comparable to the standard version. The impact of one tuning parameter (minimal width of the total water mixing ratio distribution) is reduced by using a more physical turbulent diffusion.

ACPD
11, 1971–2023, 2011

The impact of the explicit entrainment closure on ECHAM5-HAM (version ENTR, based on MCV) is evaluated, first in a single column model (SCM) study based on the ASTEX campaign, and then on the global scale. The results of the various SCM simulations are quite different. The highest values of TKE in ENTR are more in the range of observations than the huge values in STD and MCV. Moreover the highest values of TKE in STD are in a narrow time interval before midnight, though the values are more constant during the night for ENTR. In addition the strong increase of TKE during the night takes place at the cloud base in STD, but it should be at the cloud top due to radiative cooling in typical stratocumulus. This feature is reproduced nicely in ENTR. Finally the diurnal cycle simulated in cloud cover or equivalently in cloud water is much more representative in terms of TKE of observed subtropical stratocumuli in ENTR than in STD. On the other hand, the TKE is not well distributed vertically.

The mean night profile of θ_l is more stable in ENTR than in MCV in the SCM. In the SCM and in the mean profile of the Californian stratocumulus region extracted from a GCM, the inversion is decreased by the entrainment parameterization. This is physically understandable in a coarse resolution model but should be studied further. Indeed GCMs already have problems handling sharp inversions because of their coarse resolution.

ECHAM5, among others, overestimates the sensitivity of LWP to AOD partly due to a too strong Albrecht's effect (Quaas et al., 2009). An improvement of this simulated sensitivity in the GCMs is needed to increase the confidence in the prediction of the future climate, in particular the effect if the aerosols on the climate. ENTR shows a reduction of the sensitivity of LWP when the number of cloud droplets increases in a SCM sensitivity study. This is done indirectly as the entrainment closure does not depend explicitly on the number of cloud droplets.

The Pacific cross-section described by Teixeira et al. (2009) was also analyzed. The most interesting information is that the entrainment parameterization leads to an enhanced triggering of convection, following an enhanced latent heat flux due to a dryer surface layer in shallow cumulus regions. ENTR shows a transition from shallow cu-

ACPD
11, 1971–2023, 2011

mulus to stratocumulus more comparable to the observations in terms of cloud cover, but simulates fewer clouds in stratocumulus regions, which is not in agreement with observations.

Tests were done to apply just a mean entrainment velocity over the whole grid-box (instead of averaging the turbulent fluxes) which gives similar results as those presented here. However, from a theoretical point of view, it is more attractive to use our more physical approach. To take the spatial variability into account, a mean entrainment rate could be computed using the statistical information carried by the statistical cloud cover scheme by Tompkins (2002). Although it seems to be an attractive approach, it asked for more assumptions, as the PDF in the sub-grid-box directly above the cloud is not known.

Further work will concentrate on coupling the explicit entrainment parameterization presented here with a local increase of resolution where the inversion can be reconstructed consistently, and all processes computed on a finer subgrid, similar to the approach used by Grenier and Bretherton (2001) and by Lock (2001). This should first help avoiding unphysical "numerical" entrainment (due to the numerical treatment of the inversions in subsiding environment) described by Lenderink and Holtslag (2000) and second avoid the decrease of the inversion we observe with the cloud-top entrainment parameterization.

Acknowledgements. The author would like to thank Francesco Isotta, Bjorn Stevens and Johannes Quaas for very enlightening discussions during this work. We acknowledge funding from EUCAARI (European Integrated project on Aerosol Cloud Climate and Air Quality interactions) No 03683302 and the Swiss National Supercomputing Centre (CSCS) for computing time.

ACPD

11, 1971–2023, 2011

References

Ackermann, A., Kirkpatrick, M., Stevens, D., and Toon, O.: The impact of humidity above stratiform clouds on indirect aerosol climate forcing, Nature, 432, 1014–1017, 2004. 1973, 1974, 1994

Albrecht, B.: Aerosols, cloud microphysics, and fractionnal cloudiness, Science, 245, 1227–1230, 1989. 1973

Albrecht, B., Bretherton, C. S., Johnson, D., Schubert, W., and Frisch, A.: The Atlantic stratocumulus transition experiment – ASTEX, B. Am. Meteorol. Soc., 76, 889–904, 1995. 1989

Blackadar, A. K.: The vertical distribution of wind and turbulent exchange in a neutral atmosphere, J. Geophys. Res., 67, 3095–3102, 1962. 1976

Blaskovic, M., Davies, R., and Snider, J. B.: Diurnal-variation of marine stratocumulus over San-Nicolas-Island during July 1987, Mon. Weather Rev., 119, 1469–1478, 1991. 1972

Bony, S. and Dufresne, J. L.: Marine boundary layer clouds at the heart of tropical cloud feedback uncertainties in climate models, Geophys. Res. Lett., 32, L20806, doi:10.1029/2005GL023851, 2005. 1972

Bretherton, C. S. and Park, S.: A new moist turbulence parametrization in the community atmosphere model, J. Climate, 22, 3422–3448, 2009. 1975, 1987

Bretherton, C. S., Uttal, T., Fairall, C., Yutter, S., Weller, R., Baumgardner, D., Comstock, K., Wood, R., and Raga, G.: The EPIC 2001 stratocumulus study, B. Am. Meteorol. Soc., 85, 967–977, 2004. 1972, 1973, 1980, 1991, 2010

Bretherton, C. S., Blossey, P. N., and Uchida, J.: Cloud droplet sedimentation, entrainment efficiency, and subtropical stratocumulus albedo, Geophys. Res. Lett., 34, L03813, doi:10.1029/2006GL027648, 2007. 1974

Brinkop, B. and Roeckner, E.: Sensitivity of a general circulation model to parametrizations of cloud-turbulence interactions in the atmospheric boundary layer, Tellus, 47A, 197–220, 1995. 1976

Cheinet, S. and Teixeira, J.: A simple formulation for the eddy-diffusivity parametrization of cloud-topped boundary layers, Geophys. Res. Lett., 30, 1930, doi:10.1029/2003GL017377, 2003. 1984, 1985

Ciesielski, P. E., Schubert, W. H., and Johnson, R. H.: Diurnal variability of the marine boundary layer during ASTEX, J. Atmos. Sci., 58, 2355–2376, 2001. 1972

Deardorff, J. W.: On the entrainment rate of a stratocumulus-topped mixed layer, Q. J. Roy.

ACPD
11, 1971–2023, 2011

Meteor. Soc., 102, 563–582, 1976. 1987, 1989, 1994
Deardorff, J. W.: Stratocumulus-capped mixed layers derived from a three-dimensional model, Bound.-Lay. Meteorol., 18, 495–527, 1980. 1977
Duynkerke, P. G.: available at: http://www.phys.uu.nl/~wwwimau/old/ASTEX/astexcomp.html, 1996. 1989
Duynkerke, P. G. and Hignett, P.: Simulation of diurnal variation in a stratocumulus-capped marine boundary layer during FIRE, Mon. Weather Rev., 121, 3291–3300, 1993. 1993
Duynkerke, P. G., Jonker, P. J., Chlond, A., Zanten, M. C. V., Cuxart, J., Clark, P., Sanchez, E., Martin, G., Lenderink, G., and Teixeira, J.: Intercomparison of Three- and one-Dimensional Model Simulations and Aircraft Observations of Stratocumulus, Bound.-Lay. Meteor., 92, 453–487, 1999. 1990
Grenier, H. and Bretherton, C. S.: A moist parametrization for large-scale models and its application to subtropical cloud-topped marine boundary layers, Mon. Weather Rev., 129, 357–377, 2001. 1982, 2001
Hartmann, D. L., Ockert-Bell, M. E., and Michelsen, M. L.: The effect of cloud type on Earth's energy balance: global analysis, J. Climate, 5, 1281–1304, 1992. 1972
Heus, T., van Dijk, G., Jonker, H. J. J., and van den Akker, A.: Mixing in shallow cumulus clouds studied by Lagrangian particle tracking, J. Atmos. Sci., 65, 2581–2597, doi:10.1175/JAS2572.1, 2008. 1982
Hignett, P.: Observations of diurnal variation in a cloud-capped marine boundary layer, J. Atmos. Sci., 48, 1474–1482, 1991. 1972, 1991
Hill, A. A., Dobbie, S., and Ying, Y.: The impact of aerosols on non-precipitating marine stratocumulus, Part I: Model description and prediction of the indirect effect, Q. J. Roy. Meteor. Soc., 134, 1143–1154, 2008. 1974
Isotta, F., Spichtinger, P., and Lohmann, U.: Improvement and implementation of a parameterization for shallow cumulus in the global climate model ECHAM5-HAM, J. Atmos. Sci., in press, 2011. 1982
Klein, S. and Hartmann, D.: The seasonal cycle of low stratiform clouds, J. Climate, 6, 1587–1606, 1993. 1983, 1995
Köhler, M.: Improved prediction of boundary layer clouds, ECMWF Newsletter, 104, 18–22, http://www.ecmwf.int/publications/newsletters/pdf/104.pdf, 2005. 1975, 1996
Lenderink, G. and Holtslag, A. M.: Evaluation of the kinetic energy approach for modeling turbulent fluxes in stratocumulus, Mon. Weather Rev., 128, 244–258, 2000. 1992, 2001

ACPD
11, 1971–2023, 2011

Lenderink, G., van Meijgaard, E., and Holtslag, A. M.: Evaluation of the ECHAM4 cloud-turbulence scheme for stratocumulus, Meteorol. Z., 9, 41–47, 2000. 1974
Lock, A. P.: The parametrization of entrainment in cloudy boundary layers, Q. J. Roy. Meteor. Soc., 124, 2729–2753, 1998. 1975, 1986
Lock, A. P.: The numerical representation of entrainment in parametrizations of boundary layer turbulent mixing, Mon. Weather Rev., 129, 1148–1163, 2001. 2001
Lohmann, U., Stier, P., Hoose, C., Ferrachat, S., Kloster, S., Roeckner, E., and Zhang, J.: Cloud microphysics and aerosol indirect effects in the global climate model ECHAM5-HAM, Atmos. Chem. Phys., 7, 3425–3446, doi:10.5194/acp-7-3425-2007, 2007. 1976
Moeng, C.: Entrainment rate, cloud fraction, and liquid water path of PBL stratocumulus clouds, J. Atmos. Sci., 57, 3627–3643, 2000. 1986
Neggers, R. A. J., Neelin, J. D., and Stevens, B.: Impact mechanisms of shallow cumulus convection on tropical climate dynamics, J. Climate, 20, 2623–2642, 2007. 1998
Nicholls, S. and Leighton, J.: An observational study of the structure of stratiform cloud sheets: Part I. Structure, Q. J. Roy. Meteor. Soc., 112, 431–460, 1986. 1983
Nicholls, S. and Turton, J.: An observational study of the structure of stratiform cloud sheets: Part II. Entrainment, Q. J. Roy. Meteor. Soc., 112, 461–480, 1986. 1983
Quaas, J., Ming, Y., Menon, S., Takemura, T., Wang, M., Penner, J. E., Gettelman, A., Lohmann, U., Bellouin, N., Boucher, O., Sayer, A. M., Thomas, G. E., McComiskey, A., Feingold, G., Hoose, C., Kristjánsson, J. E., Liu, X., Balkanski, Y., Donner, L. J., Ginoux, P. A., Stier, P., Grandey, B., Feichter, J., Sednev, I., Bauer, S. E., Koch, D., Grainger, R. G., Kirkevåg, A., Iversen, T., Seland, Ø., Easter, R., Ghan, S. J., Rasch, P. J., Morrison, H., Lamarque, J.-F., Iacono, M. J., Kinne, S., and Schulz, M.: Aerosol indirect effects – general circulation model intercomparison and evaluation with satellite data, Atmos. Chem. Phys., 9, 8697–8717, doi:10.5194/acp-9-8697-2009, 2009. 1974, 2000
Roeckner, E., Bäuml, G., Bonaventura, L., Brokopf, R., Esch, M., Giorgetta, M., Hagemann, S., Kirchner, I., Kornblueh, L., Manzini, E., Rhodin, A., Schlese, U., Schulzweida, U., and Tompkins, A.: The atmospheric general circulation model ECHAM5, Part I: Model description, Tech. Rep. 349, Max-Planck-Institute for Meteorology, Hamburg, Germany, 2003. 1976
de Roode, S. R. and Duynkerke, P. G.: Observed Lagrangian transition of stratocumulus into cumulus during ASTEX: mean state and turbulence structure, J. Atmos. Sci., 54, 2157–2173, 1997. 1989, 1990, 1993, 2019
de Roode, S., Lenderink, G., and Köhler, M.: The representation of entrainment in

ACPD
11, 1971–2023, 2011

stratocumulus-topped boundary layers with a TKE model, unpublished, 2006. 1983
Rossow, W. B. and Schiffer, R. A.: Advances in understanding clouds from ISCCP, B. Am. Meteorol. Soc., 80, 2261–2287, 1999. 1981, 2011
von Salzen, K. and McFarlane, N. A.: Parameterization of the bulk effects of lateral and cloud-top entrainment in transient shallow cumulus clouds, J. Atmos. Sci., 59, 1405–1430, 2002. 1982
von Salzen, K., McFarlane, N., and Lazare, M.: The role of shallow convection in the water and energy cycles of the atmosphere, Clim. Dynam., 25, 671–688, 2005. 1998
Sandu, I.: Impact de l'aérosol sur le cycle de vie des nuages de couche limite, Ph.D. thesis, Université de Toulouse III – Paul Sabatier, 2007. 1973
Sandu, I., Brenguier, J.-L., Geoffroy, O., Thouron, O., and Masson, V.: Aerosol impact on the diurnal cycle of marine stratocumulus, J. Atmos. Sci., 65, 2705–2718, 2008. 1974
Sandu, I., Brenguier, J.-L., Thouron, O., and Stevens, B.: How important is the vertical structure for the representation of aerosol impacts on the diurnal cycle of marine stratocumulus?, Atmos. Chem. Phys., 9, 4039–4052, doi:10.5194/acp-9-4039-2009, 2009. 1974, 1986
Schulz, J. P., Dümenil, L., and Polcher, J.: On the land surface-atmosphere coupling and its impact in a single-column atmospheric model, J. Appl. Meteorol., 40, 642–663, 2001. 1976
Simmons, A., Uppala, S., Dee, D., and Kobayashi, S.: ERA-Interim: new ECMWF reanalysis products from 1989 onwards, ECMWF Newsletter, 110, 25–35, http://www.ecmwf.int/publications/newsletters/pdf/110.pdf, 2006. 1996
Stephens, G.: Cloud feedbacks in the climate system: a critical review, J. Climate, 18, 237–273, 2005. 1972
Stevens, B.: Entrainment in stratocumulus-topped mixed layers, Q. J. Roy. Meteor. Soc., 128, 2263–2690, 2002. 1986, 1987
Stevens, B., Lenschow, D., Vali, G., Gerber, H., Bandy, A., Blomquist, B., Campos, T., Faloona, I., Haimov, S., Lilly, D., Morley, B., Thorton, D., and Moeng, C.-H.: On entrainment rates in nocturnal marine stratocumulus, Q. J. Roy. Meteor. Soc., 129, 3469–3493, 2003. 1993
Stevens, B., Moeng, C. H., Ackerman, A. S., Bretherton, C. S., Chlond, A., De Roode, S., Edwards, J., Golaz, J. C., Jiang, H. L., Khairoutdinov, M., Kirkpatrick, M. P., Lewellen, D. C., Lock, A., Muller, F., Stevens, D. E., Whelan, E., and Zhu, P.: Evaluation of large-Eddy simulations via observations of nocturnal marine stratocumulus, Mon. Weather Rev., 133, 1443–1462, 2005. 1973, 1974

ACPD
11, 1971–2023, 2011

Stier, P., Feichter, J., Kinne, S., Kloster, S., Vignati, E., Wilson, J., Ganzeveld, L., Tegen, I., Werner, M., Balkanski, Y., Schulz, M., Boucher, O., Minikin, A., and Petzold, A.: The aerosol-climate model ECHAM5-HAM, Atmos. Chem. Phys., 5, 1125–1156, doi:10.5194/acp-5-1125-2005, 2005. 1976

Sundqvist, H., Berge, E., and Kristjansson, J.: Condensation and cloud parametrization studies with a mesoscale numerical weather prediction model, Mon. Weather Rev., 117, 1641–1657, 1989. 1978

Teixeira, J., Cardoso, S., Bonazzola, M., Cole, J., DelGenio, A., DeMott, C., Franklin, C., Hannay, C., Jakob, C., Jiao, Y., Karlsson, J., Kitagawa, H., Köhler, M., Kuwano-Yoshida, A., Le Drian, C., Lock, A., Miller, M., Marquet, P., Martins, J., Mechoso, C. R., v. Meijgaard, E., Meinke, I., Miranda, P., Mironov, D., Neggers, R., Pan, H., Randall, D., Rasch, P., Rockel, B., Rossow, W. B., Ritter, B., Siebesma, A., Soares, P., Turk, F., Vaillancourt, P., Engeln, A. V., and Zhao, M.: Tropical and sub-tropical cloud transitions in weather and climate prediction models: the GCSS/WGNE Pacific cross-section intercomparison (GPCI), J. Climate, submitted, 2009. 1996, 1998, 2000, 2022, 2023

Tiedtke, M.: A comprehensive mass flux scheme for cumulus parameterization in large-scale models, Mon. Weather Rev., 117, 1779–1800, 1989. 1997

Tiedtke, M., Heckley, W. A., and Slingo, J.: Tropical forecasting at ECMWF: the influence of physical parametrization on the mean structure of forecasts and analyses, Q. J. Roy. Meteor. Soc., 114, 639–664, 1988. 1998

Tompkins, A.: A prognostic parametrization for the subgrid-scale variability of water vapor and clouds in large scale models and its use to diagnose cloud cover, J. Atmos. Sci., 59, 1917–1942, 2002. 1978, 1979, 1981, 1999, 2001, 2008, 2009

Turton, J. D. and Nicholls, S.: A study of the diurnal variation of stratocumulus using a multiple mixed layer model, Q. J. Roy. Meteor. Soc., 113, 969–1009, 1987. 1986, 1987, 1999, 2008

Twomey, S.: The influence of pollution on the shortwave albedo of clouds, J. Atmos. Sci., 34, 1149–1152, 1977. 1973

Uppala, S., Kallberg, P., Simmons, A., Andrae, U., Bechtold, V., Fiorino, M., Gibson, J., Haseler, J., Hernandez, A., Kelly, G., Li, X., Onogi, K., Saarinen, S., Sokka, N., Allan, R., Andersson, E., Arpe, K., Balmaseda, M., Beljaars, A., van de Berg, L., Bidlot, J., Bormann, N., Caires, S., Chevallier, F., Dethof, A., Dragosavac, M., Fisher, M., Fuentes, M., Hagemann, S., Holm, E., Hoskins, B., Isaksen, L., Janssen, P., Jenne, R., McNally, A., Mahfouf, J., Morcrette, J., Rayner, N., Saunders, R., Simon, P., Sterl, A., Trenberth, K., Untch, A.,

ACPD
11, 1971–2023, 2011

Vasiljevic, D., Viterbo, P., and Woollen, J.: The ERA-40 re-analysis, Q. J. Roy. Meteor. Soc., 131, 2961–3012, doi:10.1256/qj.04.176, 2005. 1996

Wood, R.: Cancellation of aerosol indirect effects in marine stratocumulus through cloud thinning, J. Atmos. Sci., 64, 2657–2669, 2007. 1973

van Zanten, M. C., Stevens, B., Vali, G., and Lenschow, D. H.: Observations of drizzle in nocturnal marine stratocumulus, J. Atmos. Sci., 62, 88–106, doi:10.1175/JAS-3355.1, 2005. 1973

ACPD

11, 1971–2023, 2011

Table 1. Acronyms of the different simulations.

Simulation	Description
STD	Standard ECHAM5-HAM, using the statistical cloud cover scheme by Tompkins (2002).
RED	As simulation STD, but with reduced minimal width threshold of the PDF in order to separate the liquid water mixing ratio accurately from the total water mixing ratio.
MCV	As simulation RED, but with the turbulent diffusion applied to adiabatically conserved variables.
ENTR	As simulation MCV, but with the explicit entrainment parameterization of Turton and Nicholls (1987), applied at cloud tops in stratocumulus regions.

ACPD
11, 1971–2023, 2011

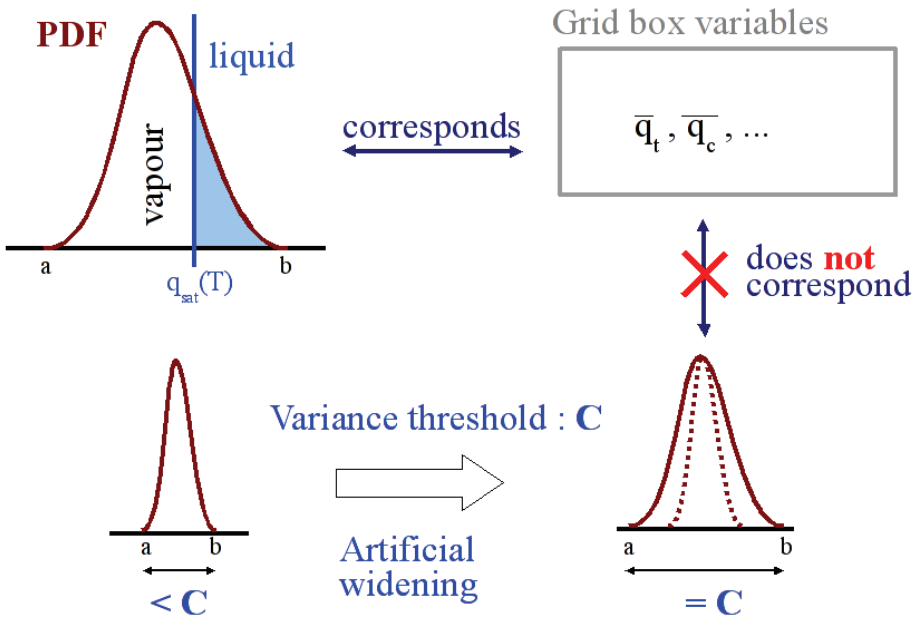

Fig. 1. Sketch of process of widening the probability density function (PDF) done in the cloud cover scheme by Tompkins (2002). Theoretically the PDF of the total mixing ratio corresponds to the mean grid mixing ratios of the grid box. When the PDF is narrower than a variance threshold $C \cdot q_v$, the PDF is artificially widened. This widening does not affect the mixing ratios as they depend on a conservation equation. Thus, the PDF does not correspond anymore to the mean mixing ratios.

ACPD
11, 1971–2023, 2011

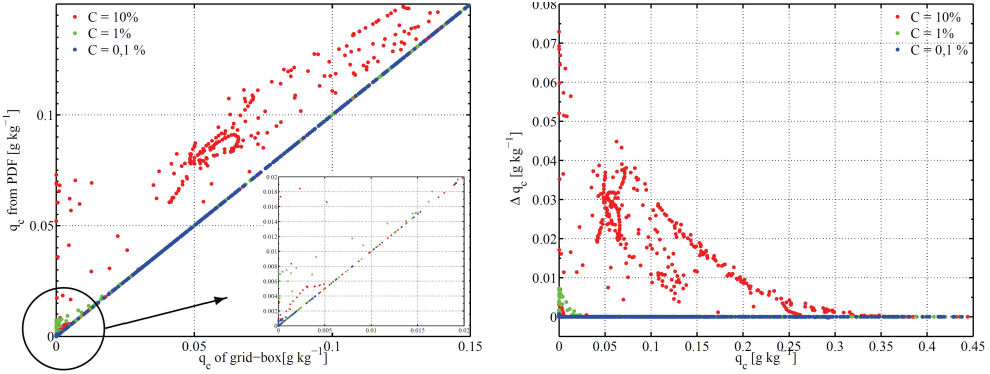

Fig. 2. Left: liquid water mixing ratio determined from the total mixing ratio PDF of the grid box (y-axis) with respect to the corresponding liquid water mixing ratio of the grid box (x-axis) for different clouds simulated by ECHAM5-HAM for the EPIC campaign (Bretherton et al., 2004) for various values of C. Right: difference between the PDF determined and grid-box liquid water mixing ratio for the EPIC campaign.

ACPD
11, 1971–2023, 2011

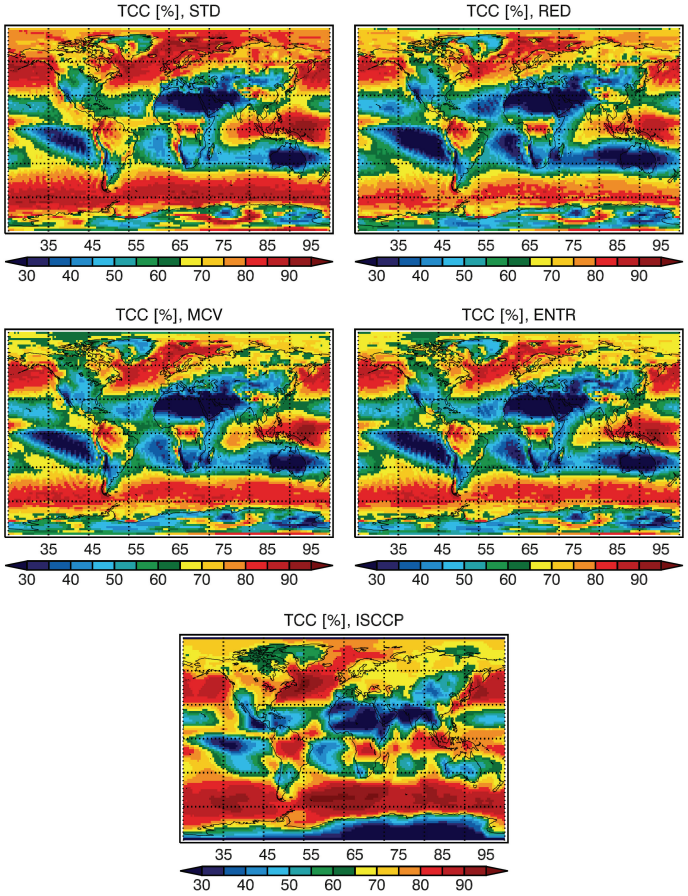

Fig. 3. Three years averaged annual mean total cloud cover (TCC, %) for experiments STD, RED, MCV and ENTR (see Table 1). Lower panel: observations from International Satelite Cloud Climatology Project (ISCCP, averaged over the period from 1983 to 2005) (Rossow and Schiffer, 1999).

ACPD
11, 1971–2023, 2011

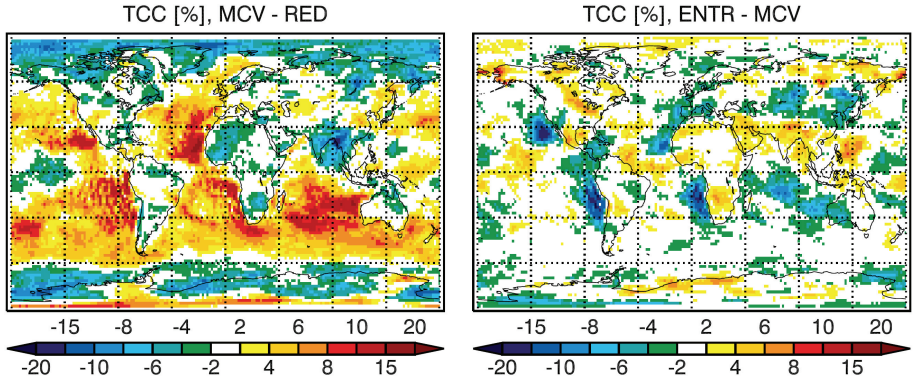

Fig. 4. Differences between the experiment MCV-RED and ENTR-MCV (three years averaged).

ACPD
11, 1971–2023, 2011

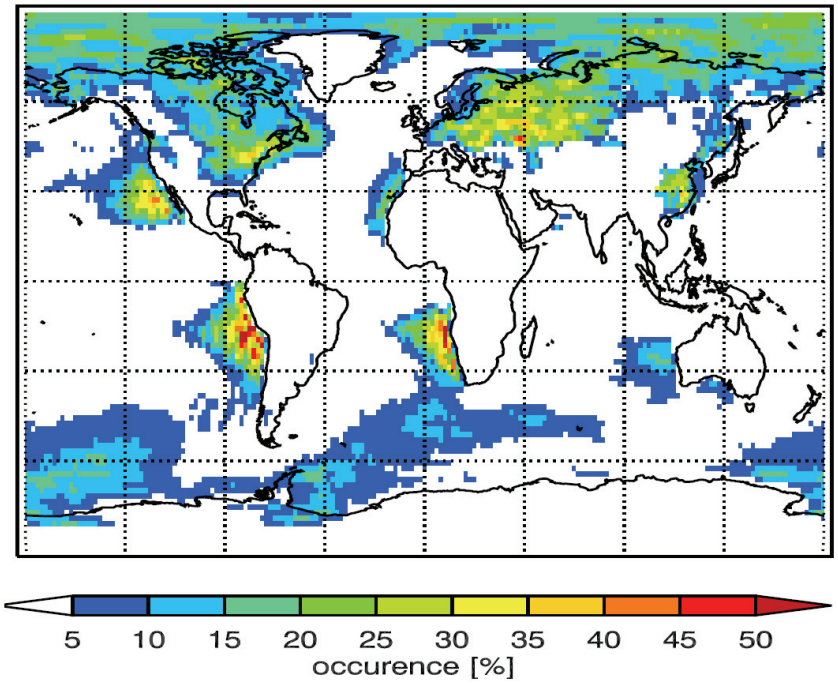

Fig. 5. Annual frequency of meeting the criterion for cloud-top entrainment in ECHAM5-HAM as described in Sect. 3.2.

ACPD
11, 1971–2023, 2011

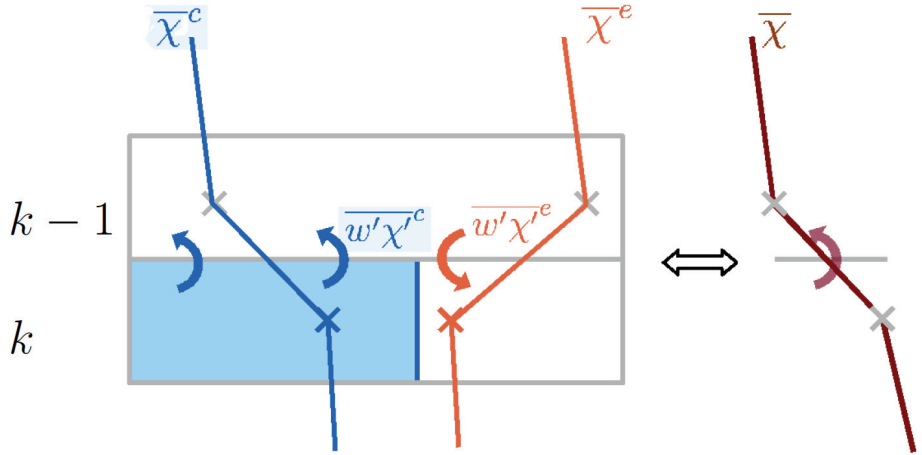

Fig. 6. Schematic picture of the decomposition of the different fluxes: The mean flux of χ is now expressed in terms of the weighted mean of the two fluxes over the cloudy and clear air region. The gray boxes represent two grid-boxes one over the other, $\bar{\chi}^c$ line represents the cloud profile and $\bar{\chi}^e$ the dry profile. The $\bar{\chi}$ profile on the right is the profile of the mean variables.

ACPD
11, 1971–2023, 2011

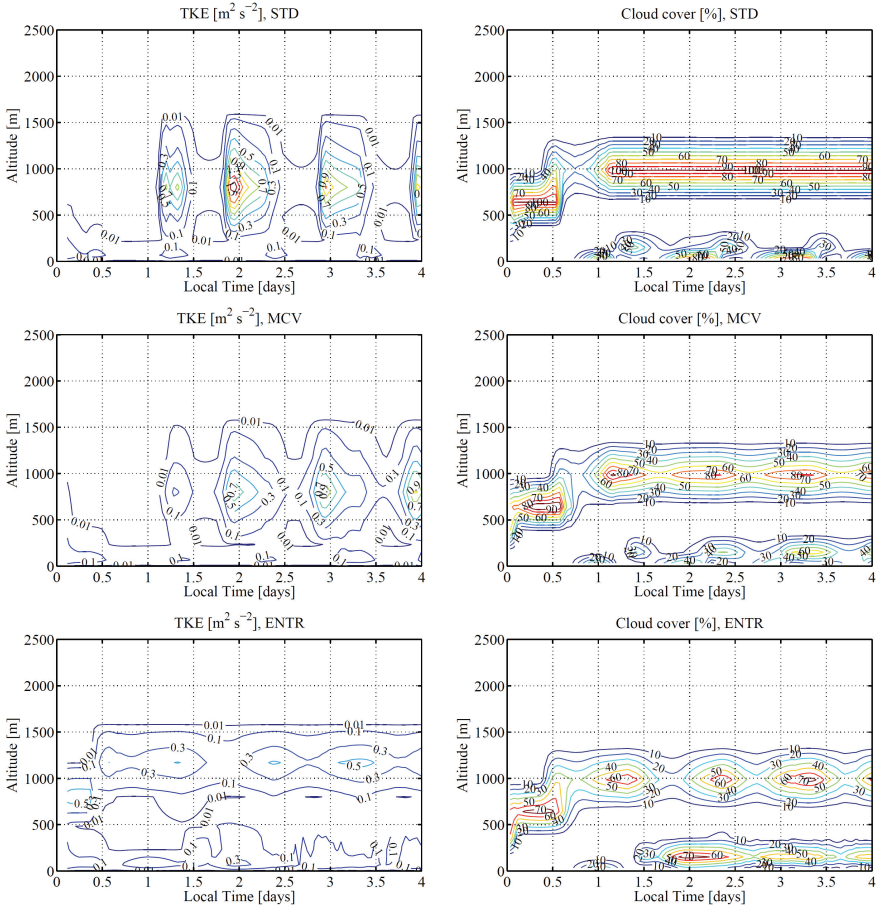

Fig. 7. Time-height contour plots of TKE ($m^2\,s^{-2}$) (left) and cloud cover (%) (right) for different versions of ECHAM5 (see Table 1) with respect to local time (days) and altitude (m) in SCM simulations of the ASTEX case.

ACPD
11, 1971–2023, 2011

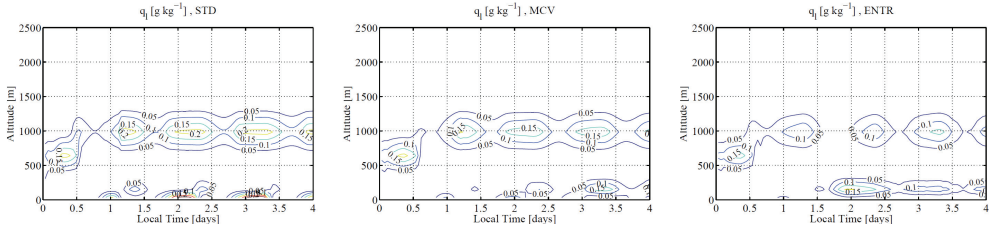

Fig. 8. Time-height contour plot of liquid mixing ratio (g kg^{-1}) in a SCM simulation of the ASTEX case for the STD, MCV and ENTR simulations.

ACPD
11, 1971–2023, 2011

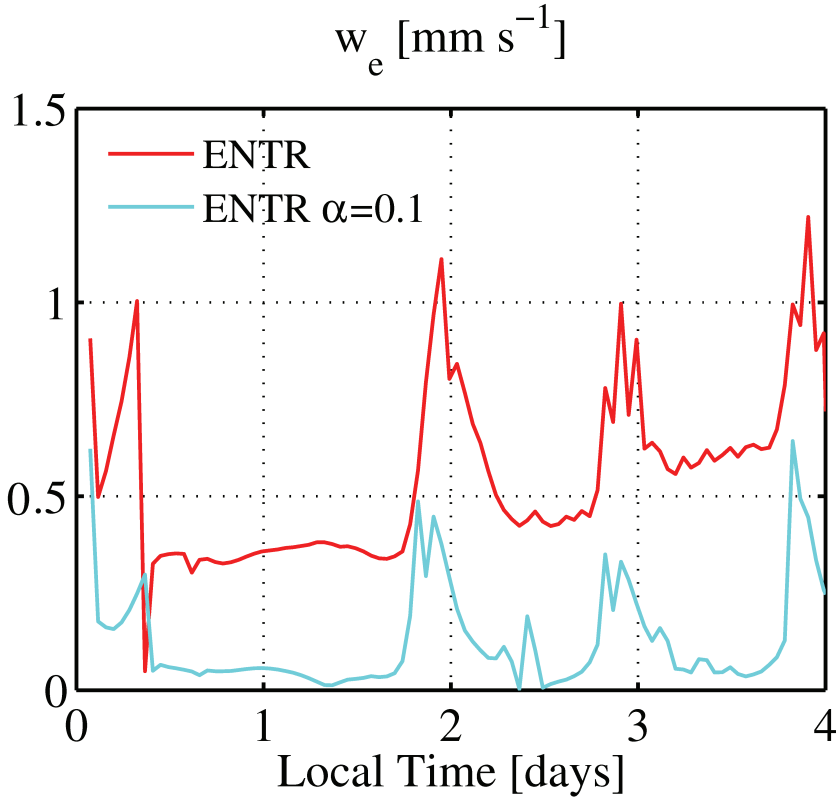

Fig. 9. Time-serie of w_e (mm s^{-1}) in a SCM simulation of the ASTEX case for simulation ENTR and for simulation ENTR with a reduced value of cloud-top radiative cooling acting on the buoyancy production.

ACPD
11, 1971–2023, 2011

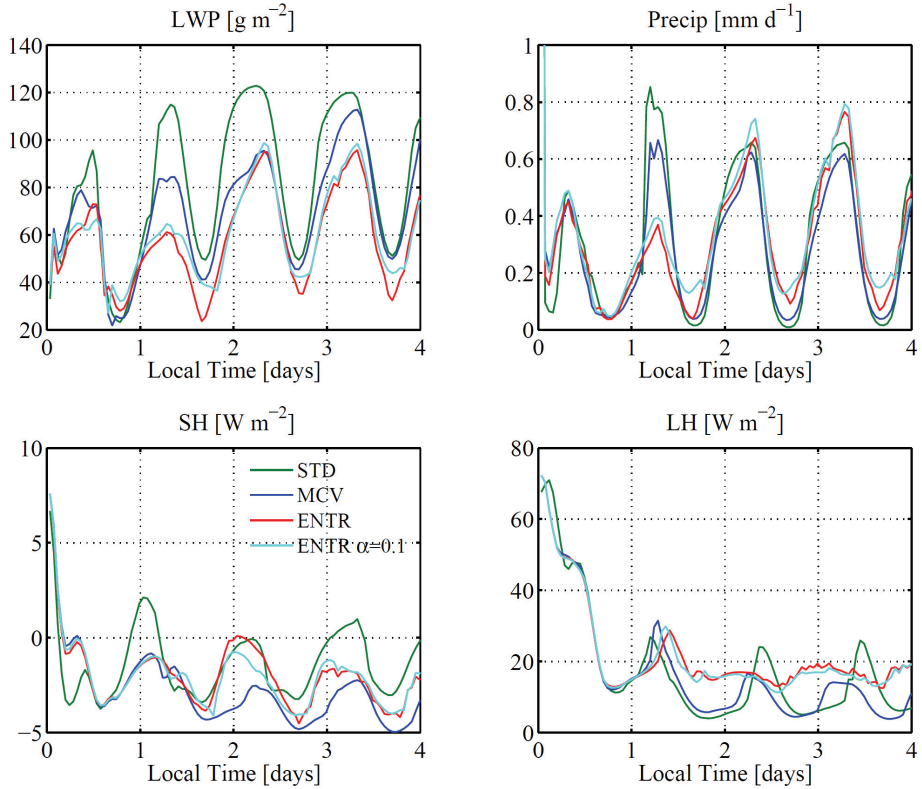

Fig. 10. Time-series of LWP (g m^{-2}), precipitation (mm d^{-1}), sensible (SH) and latent heat (LH) fluxes (W m^{-2}) in a SCM simulation of the ASTEX case for the four simulations STD, MCV, ENTR and ENTR with $\alpha = 0.1$.

ACPD
11, 1971–2023, 2011

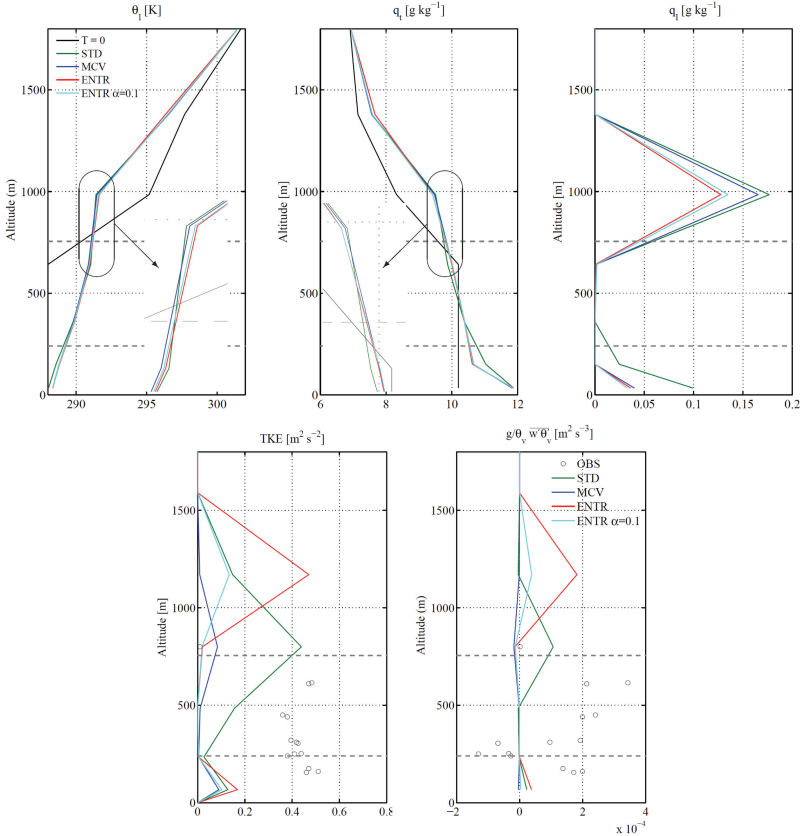

Fig. 11. Mean profiles during night of the first day (corresponding to day 1–1,25 of Fig. 7) from the SCM simulations of the ASTEX campaign. Upper panel: liquid potential temperature θ_l, q_t and q_l). Lower panel: TKE and buoyancy production $\frac{g}{\theta_v}\overline{w'\theta'_v}$. The horizontal dashed black lines show the observed cloud top and base while circles represent observations reported by de Roode and Duynkerke (1997).

ACPD
11, 1971–2023, 2011

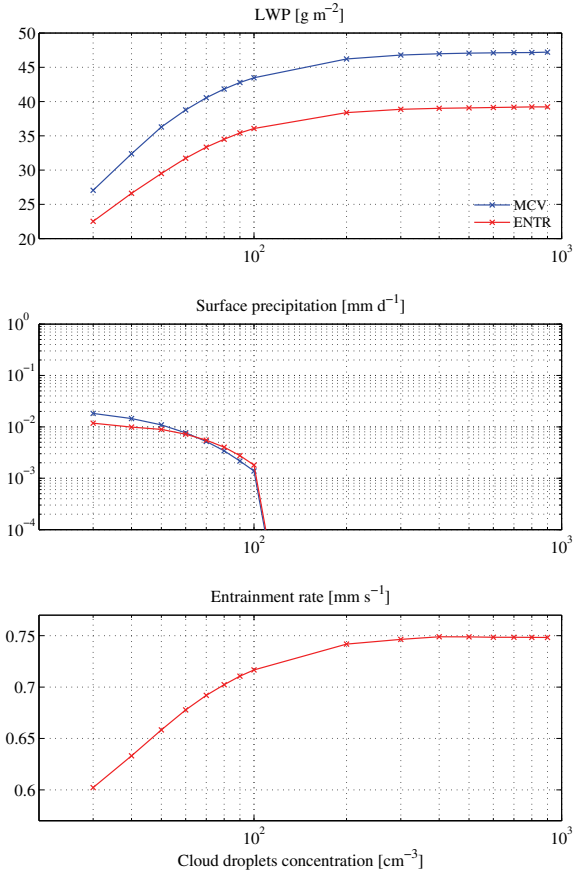

Fig. 12. Liquid water path (g kg^{-1}), surface precipitation (mm d^{-1}) and computed entrainment rate (mm s^{-1}) with respect to cloud droplet number concentration. Average over the 2nd hour of simulation of the ASTEX case for the two simulations MCV and ENTR.

ACPD
11, 1971–2023, 2011

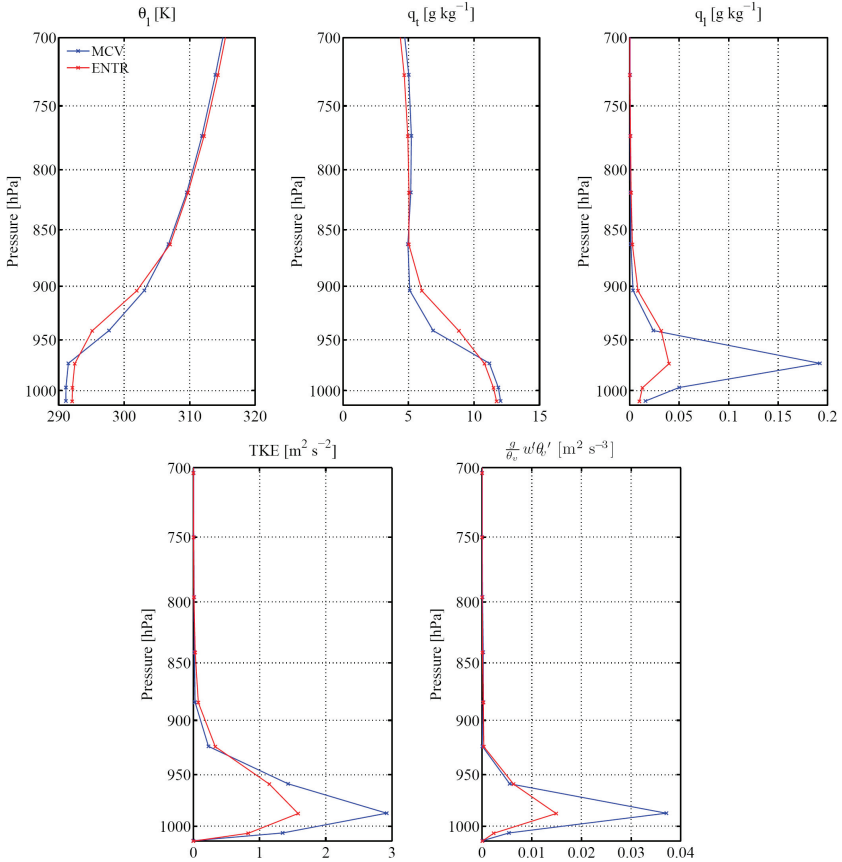

Fig. 13. Mean JJA vertical profiles of three years simulations over the Californian stratocumulus region (20° N–30° N, 120° W–130° W) from simulations MCV and ENTR. Upper panel: liquid potential temperature θ_l, q_t and q_l. Lower panel: TKE and buoyancy production $\frac{g}{\theta_v}\overline{w'\theta'_v}$.

ACPD
11, 1971–2023, 2011

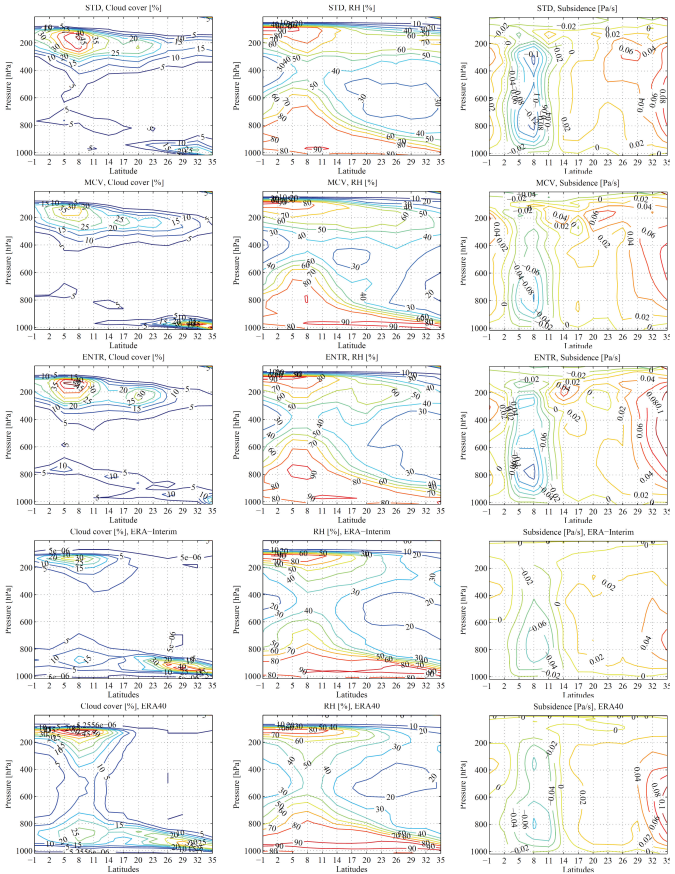

Fig. 14. Contour plot of cloud cover (%), relative humidity (%) and subsidence ($Pa\,s^{-1}$) along the Pacific cross-section (Teixeira et al., 2009). Three first rows: simulations STD, MCV and ENTR averaged over JJA in a 3-D climatological simulation. Two lower rows: averaged over JJA 2000 from 12-hourly data for ERA-Interim and for ERA40.

ACPD
11, 1971–2023, 2011

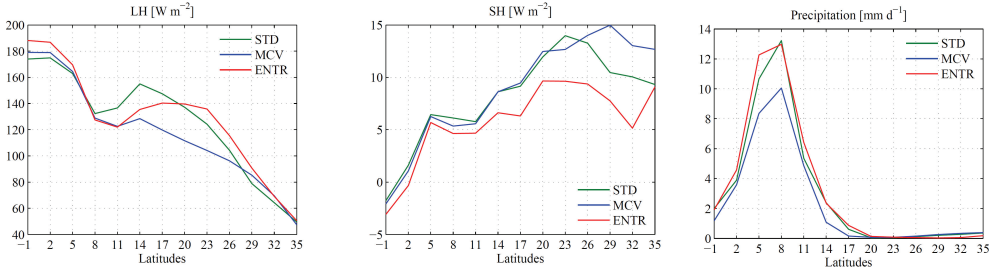

Fig. 15. Latent and sensible surface fluxes (W m^{-2}) and precipitation (mm d^{-1}) averaged over JJA 2000 (climatological simulation) along the Pacific cross-section (Teixeira et al., 2009) for the STD, MCV and ENTR versions.

ACPD
11, 1971–2023, 2011